Citalopram exhibits immune-dependent anti-tumor effects by modulating C5aR1^{+} TAMs and CD8^{+} T cells

Fangyuan Dong[1, 3, 4, 5, 11], Shan Zhang[2, 11], Kaiyuan Song[6, 11], Luju Jiang[2, 11], Li-Peng Hu[2], Qing Li[2], Xue-Li Zhang[2], Jun Li[2], Mingxuan Feng[7], Zhi-Wei Cai[8], Hong-Fei Yao[8], Rong-Kun Li[9], Hui Li[2], Jie Chen[1, 3, 4, 5], Xiaona Hu[1, 3, 4, 5], Jiaofeng Wang[1, 3, 4, 5], Chongyi Jiang[8], Helen He Zhu[10], Cun Wang[2], Lin-Tai Da[6], Zhi-Gang Zhang[2, #], Zhijun Bao[1, 3, 4, 5, #], Xu Wang[9, #], Shu-Heng Jiang[2, #]

[1]Department of Gastroenterology, Huadong Hospital, Shanghai Medical College, Fudan University, Shanghai 200040, P.R. China

[2]State Key Laboratory of Systems Medicine for Cancer, Shanghai Cancer Institute, Ren Ji Hospital, School of Medicine, Shanghai Jiao Tong University, Shanghai 200240, P.R. China

[3]Shanghai Key Laboratory of Clinical Geriatric Medicine, Shanghai 200040, P.R. China

[4]National Clinical Research Center for Aging and Medicine, Shanghai 200040, P.R. China

[5]Department of Geriatrics, Huadong Hospital, Shanghai Medical College, Fudan University Shanghai 200040, P.R. China

[6]Key Laboratory of Systems Biomedicine (Ministry of Education), Shanghai Center for Systems Biomedicine, Shanghai Jiao Tong University, Shanghai 200240, China

[7]Department of Liver Surgery, Ren Ji Hospital, School of Medicine, Shanghai Jiao Tong University, Shanghai 200127, P.R. China

[8]Department of General Surgery, Hepato-biliary-pancreatic Center, Huadong Hospital, Fudan University, Shanghai 200040, P.R. China

[9]Institute of Oncology, Affiliated Hospital of Jiangsu University, Zhenjiang 212001, P.R. China

[10]State Key Laboratory of Systems Medicine for Cancer, Renji-Med-X Stem Cell Research Center, Shanghai Cancer Institute & Department of Urology, Ren Ji Hospital, Shanghai Jiao Tong University School of Medicine, Shanghai, 200127, China;

[11]These authors contributed equally to this work

[#]**Correspondence**

shjiang@shsci.org (S.H.J.); zhijunbao@fudan.edu.cn (Z.B.); wangxu@ujs.edu.cn (X.W.); zzhang@shsci.org (Z.G.Z).

Abstract

Administration of selective serotonin reuptake inhibitors (SSRIs) is associated with a reduced cancer risk and shows significant anti-tumor effects across multiple tumor types, suggesting the potential for repurposing SSRIs in cancer therapy. Nonetheless, the specific molecular target and mechanism of action of SSRIs remain to be fully elucidated. Here, we reveal that citalopram exerts an immune-dependent anti-tumor effects in hepatocellular carcinoma (HCC). Interestingly, the anti-HCC effects of citalopram are not reliant on its conventional target, the serotonin transporter. Through various drug repurposing approaches, including global reverse gene expression profiling, drug affinity responsive target stability assay, and molecular docking, the complement component 5a receptor 1 (C5aR1) is identified as a new target of citalopram. C5aR1 is predominantly expressed by tumor-associated macrophages (TAMs), and citalopram treatment enhances local macrophage phagocytosis and elicits $CD8^+$ T anti-tumor immunity. At a systemic level, citalopram treatment results in decreased serum 5-HT levels, which correlates with increased activation of $CD8^+$ T cells. Additionally, citalopram promotes αCD3/αCD28-stimulated $CD8^+$ T cell activation, expansion, and cytotoxicity. Depletion of $CD8^+$ T cells partially hinders the anti-HCC effects of citalopram. Collectively, our study reveals multiple immunomodulatory roles of citalopram in inducing anti-tumor immunity, and provides a basis for considering the repurposing of SSRIs as promising anticancer agents for HCC treatment.

Key words: Drug repurposing, Drug discovery, SLC6A4, SERT, Anti-tumor immunity

Introduction

The development of anti-tumor drugs encounters numerous challenges, such as a high failure rate, substantial costs, limited bioavailability, safety concerns, and lengthy design and testing procedures [1]. As different diseases may share common pathological mechanisms, there is a growing focus on repurposing existing drugs for new applications, referred to as “new uses for old drugs” [2, 3]. Additionally, exploring new disease-relevant targets for established drugs and broadening their indications offers significant translational value [4].

Selective serotonin reuptake inhibitors (SSRIs; i.e., citalopram, escitalopram, fluoxetine, fluvoxamine, paroxetine, and sertraline) are frequently prescribed to treat conditions such as depression, anxiety, insomnia, and chronic pain [5]. SSRIs target the serotonin transporter (SERT, encoded by the *SLC6A4* gene), blocking the reuptake of serotonin (5-hydroxytryptamine, 5-HT) into the presynaptic neuron, ultimately increasing 5-HT levels in the brain [6]. Recent population-based epidemiological studies suggest that SSRIs have the potential to reduce the risk of many cancers, including kidney, breast, colorectal, and liver cancers [7-10]. The anxiety and depression symptoms among cancer patients is increasingly recognized [11]. Considering the established safety profile and known side effects of SSRIs, repurposing these drugs as potential anti-tumor agents, particularly for cancer patients with comorbid depression, could offer dual benefits. This approach may not only help improve neurological function but also potentially impede tumor progression. Hence, repurposing SSRIs in this context could present a cost-effective option. Nevertheless, the mechanisms of actions responsible for the anti-tumor effects of SSRIs are still largely unknown.

In this study, using hepatocellular carcinoma (HCC) as a model, we revealed that citalopram, an SSRI, exhibits anti-tumor properties not through its traditional target SERT, but instead via partially immune-dependent mechanisms. Through a comprehensive approach involving global reverse gene expression profiling, drug affinity responsive target stability (DARTS) [12], and molecular docking analyses, we identified the complement component 5a receptor 1 (C5aR1), predominantly expressed by tumor-associated macrophages (TAMs), as a target of citalopram. C5aR1 play critical roles in fostering an immunosuppressive microenvironment [13, 14] and boosting the metastatic potential of cancer cells [15]. Given its significant impact on cancer progression, C5aR1 has surfaced as a promising therapeutic

target for potential cancer interventions. Here, we further elucidated the mechanism underlying the connection between C5aR1^{+} TAMs and citalopram-related phenotypes. Additionally, after citalopram treatment, a decline in serum 5-HT levels was observed, which is linked to the activation of CD8^{+} T cells. More importantly, citalopram directly stimulates CD8^{+} T cell activation, expansion, and cytotoxicity under *in vitro* conditions. Collectively, the anti-tumor effects of citalopram in HCC involve multiple immune-dependent mechanisms.

Results

The immune-dependent anti-tumor effects of citalopram in HCC

To evaluate the therapeutic effects of citalopram, we engrafted mouse Hepa1-6 and Hep53.4 cells into different strains of recipient mice, including the immune-competent C57BL/6 mice and immune-compromised Rag1$^{-/-}$ mice. Citalopram was given by i.p. administration daily for 30 days after bearing palpable tumors (~50 mm^{3}). Tumor growth was significantly retarded in both two mouse models. Of note, this impairment was more pronounced in immune-competent C57BL/6 mice, indicating an immune-dependent effect of citalopram (Figures 1A-B). This finding was further validated at molecular levels, as evidenced by reduced staining of the proliferation index Ki67 and increased expression of cleaved caspase 3 (CCS3) (Figure S1).

As SERT is the known target of SSRIs, we tested the therapeutic effect of citalopram in the absence of SERT (Figures 1C-D). In mouse HCC cells, SERT knockdown failed to affect cell proliferation or cell apoptosis *in vitro* and *in vivo* (Figures 1E-F and S2A-B). However, citalopram delayed the growth of SERT-silenced HCC tumors, and its suppressive effect was more proficient in immune-competent hosts compared with Rag1$^{-/-}$ ones (Figures 1E-F and S2C-F). Together, these data suggest that citalopram might target other molecules instead of SERT to exhibit an immune-dependent anti-tumor effects in HCC.

C5aR1 is a direct target of citalopram

Previously, using drug-induced gene signature networks and target prediction method, we identified a repertoire of targets related to citalopram treatment [16]. The top two hits are

glucose transporter 1 (GLUT1) and C5aR1 (Figures 2A-B). Citalopram can reverse the Warburg effect to inhibit HCC by targeting GLUT1 directly [16]. Considering the significant role of C5aR1 in immune modulation [17], we investigated whether the immune-dependent anti-tumor effects of citalopram are mediated through C5aR1. Immunohistochemical analysis showed that the positive staining of C5aR1 was predominantly found in scattered immune cells (Figure 2C). Single-cell sequencing data indicated that C5aR1 was expressed at higher levels in monocytes/macrophages within the tumor microenvironment (TME) compared with other cell types (Figure 2D). Co-immunofluorescence analysi corroborated that $CD163^{+}$ macrophages presented significant C5aR1 immunoreactivity (Figure 2E).

The DARTS assay is widely recognized technique used to identify potential protein targets for small molecules. This approach involves conferring proteolytic protection of target proteins by their interaction with small molecules [18]. Combined DARTS assay with immunoblotting analysis, we investigated the stability of C5aR1 against pronase in the presence or absence of citalopram treatment. Because C5aR1 is expressed by macrophages, THP-1 cells were employed for the DARTS assay. Citalopram did not affect the basal protein level of C5aR1 in macrophages (Figure 2F). However, citalopram could enhance the stability of C5aR1 against pronase treatment. Of note, this effect was specific to C5aR1, as citalopram did not impact the proteolytic susceptibility of β-actin (Figures 2F). Moreover, the stability of C5aR1 against pronase was enhanced in a dose-dependent manner following treatment with citalopram (Figures 2G). Besides citalopram, other 5 SSRIs (escitalopram, fluoxetine, fluvoxamine, paroxetine, and sertraline) also played protective roles of C5aR1 against pronase (Figure S3A).

To address citalopram/C5aR1 interaction, *in silico* docking analysis was conducted. Previous studies revealed two different inhibitor-binding sites in C5aR1, namely, the orthosteric site on the extracellular side and the allosteric site outside the transmembrane bundle [19]. Therefore, we docked the structure of citalopram into both orthosteric and allosteric sites of human C5aR1 (PDB id: 6C1Q), respectively. *In silico* docking of citalopram into the orthosteric site predicted two binding conformations without overlap (Figures 2H and S3B). In pose-1, the fluorophenyl and the cyanophtalane group of citalopram stacked with the side chains of Y258 and R206, and the amino group of citalopram interacted with the negatively

charged residue E199 (Figure 2I, left). In pose-2, two negatively charged residues, D282 and D37, surrounded the amino group (Figure 2I, middle). Considering the accessibility, D282 orienting towards the binding cavity of C5aR1 might play a more pivotal role in the citalopram binding event proposed by pose-2. Additionally, the cyanophtalane group of citalopram interacted with hydrophobic residues L92 and P113 of C5aR1. The fluorine was inserted into a narrow space lying over the side chain of W102 (Figure 2I, right). For the allosteric site, residue W213 played a critical role in inhibitor binding via hydrogen-bond interactions established by the amino group in the indole ring [20]. According to the best pose from cluster 2, the citalopram formed a hydrogen-bond via the oxygen atom in the cyanophtalane group with W213 (Figure 2I, right). Inspired by these molecular docking results, we generated six C5aR1 mutants to figure out the real binding site of citalopram in HEK293T cells (Figure S3C). Indeed, citalopram had no protective effects on C5aR1 stability with the transfection of HA-C5aR1 E199 and D282 mutant against pronase (Figure 2J). Consistently, mutations on E199 and D282 reduce C5a binding affinity to C5aR1 [21]. Furthermore, docking analysis and DARTS assay revealed that other four SSRIs could bind to the D282 site of C5aR1 (Figures S3D-E). These findings demonstrate that SSRIs adopt the orthosteric site to bind to C5aR1 and electrostatic interactions between C5aR1 D282 and the amino groups of SSRIs play an instrumental role in the binding mechanisms.

Citalopram targets C5aR1 in tumor-associated macrophages (TAMs)

C5aR1, the receptor for anaphylatoxin C5a, is profoundly implicated in tumor progression via inducing an immunosuppressive microenvironment in which TAMs are involved [14]. As C5aR1 is localized in TAMs within the TME of HCC, we explored whether citalopram exerted anti-tumor functions by targeting C5aR1 on TAMs. Given that citalopram also targets GLUT1 in HCC [16], we generated a Hepa1-6 clone with complete knockdown of GLUT1 ($GLUT1^{KD}$) to dissect C5aR1-dependent roles (Figure 3A). Interestingly, citalopram displayed an inhibitory effect on $GLUT1^{KD}$ tumors in immune-component C57BL/6 mice but not $Rag1^{-/-}$ ones (Figure 3B), underscoring the contribution of C5aR1. To delineate the involvement of macrophages, we first depleted mouse macrophages with clodro-Liposomes and found that citalopram was ineffective in controlling $GLUT1^{KD}$ tumors (Figure S4), implying the influences of citalopram on

macrophages. As the second line of evidence, we engrafted GLUT1^{KD} Hepa1-6 cells into the syngeneic *C5ar1*$^{+/-}$ and *C5ar1*$^{-/-}$ mice. Compared with *C5ar1*$^{+/-}$ recipients, tumor growth was attenuated in *C5ar1*$^{-/-}$ recipients (Figure 3C), whereas C5a deposition remained unchanged (Figure 3D). Third, we co-injected *C5ar1*$^{+/-}$ versus *C5ar1*$^{-/-}$ bone marrow-derived macrophages (BMDMs) with GLUT1^{KD} Hepa1-6 cells into syngeneic recipient *C5ar1*$^{-/-}$ mice to analyze the therapeutic effect of citalopram. Implantation of *C5ar1*$^{+/-}$ BMDMs into *C5ar1*$^{-/-}$ recipients restored tumor growth compared with their *C5ar1*$^{-/-}$ counterparts and citalopram cannot restrict tumor growth in r*C5ar1*$^{-/-}$; d*C5ar1*$^{-/-}$ mice; in contrast, tumor growth kinetics were considerably diminished in r*C5ar1*$^{-/-}$; d*C5ar1*$^{+/-}$ mice upon citalopram treatment (Figure 3E), suggesting that C5aR1^{+} TAM rewiring enables the tumoricidal effects of citalopram. Notably, C5a deposition was not affected by citalopram treatment (Figure 3F).

To answer how C5aR1^{+} macrophages mediate citalopram-induced anti-tumor effects, we probed macrophage functions. Phagocytosis assay showed that isolated TAMs from *C5ar1*$^{-/-}$ recipients had higher phagocytic capacity of HCC cells than that of *C5ar1*$^{+/-}$ recipients (Figure 3G), and citalopram increased the phagocytosis of TAMs from r*C5ar1*$^{-/-}$; d*C5ar1*$^{+/-}$ mice (Figure 3H). Moreover, C5a-mediated macrophage phagocytic impairment was reversed by C5aR1 knockdown or treatment with citalopram or different SSRIs (Figures S5A-C). C5a was able to suppress, while citalopram was effective in bolstering phagocytosis in macrophages expressing C5aR1^{WT} but not C5aR1^{D282A} (Figures S5D-E). Despite several residues of mouse C5aR1 protein being different from that of human C5aR1, citalopram shared a similar binding model with them (Figure S6). In orthotopic GLUT1^{KD} Hepa1-6 models, flow cytometry revealed a significant reduction of TAMs in the citalopram group compared with the control group (Figure 3I). Moreover, TAM polarization was shifted to a proinflammatory state (Figure 3J). Further phenotyping of tumor immune subsets in immunocompetent C57BL/6 mice showed that citalopram increased the infiltration of CD8^{+} T and dendritic cells while decreasing the infiltration of CD4^{+} T and B220^{+} B cells (Figure 3K). No significant changes were observed in splenic immune subsets upon citalopram treatment (Figure S7).

Next, we sought to understand whether C5aR1^{+} TAMs impact on CD8^{+} T cells. Intratumoral CD8^{+} T cells from tumor-bearing *C5ar1*$^{-/-}$ mice had increased frequency and expression of GZMB, IFN-γ, and TNF-α compared with that from *C5ar1*$^{+/-}$ mice (Figure 3L).

Likewise, the frequency and cytotoxicity of CD8$^+$ T cell from r*C5ar1*$^{-/-}$; d*C5ar1*$^{+/-}$ mice were reduced compared with r*C5ar1*$^{-/-}$; d*C5ar1*$^{-/-}$ mice, and this effect was partially reversed by citalopram treatment (Figure 3M). Furthermore, depletion of CD8$^+$ T cells abrogated the effect of macrophage C5aR1 deficiency on tumor growth (Figure 3N), suggesting that CD8$^+$ T cells are needed for the pro-tumor phenotype of C5aR1$^+$ TAMs. Clinically, data from TCGA cohort reinforced the link between C5aR1 expression and an immunosuppressive TME as demonstrated by the associations with TAMs, exhausted T cells, immune checkpoint molecules, and effector Tregs (Figure 3O).

Citalopram-induced activation of CD8$^+$ T cells involves a serotonergic-dependent mechanism

Considering the fact that citalopram targets GLUT1 and CD8$^+$ T cell function is reliant on glycolytic metabolism, we investigated the *in vivo* effects of citalopram on T cells. As a result, citalopram significantly invigorated CD8$^+$ T cell function and glycolytic metabolism in intrahepatic tumors from WT C57BL/6 mice (Figures 4A-B). To simulate the role of metabolic-associated fatty liver disease (MAFLD) in the development of cirrhosis and HCC[22, 23], we fed C57BL/6 mice a choline-deficient, amino acid-defined high-fat diet (CDAHFD) to induce metabolic dysfunction-associated steatohepatitis (MASH)/fibrosis prior to orthotopic Hepa1-6 cell implantation. Likewise, CD8$^+$ T cell function and glycolytic metabolism were enhanced in MASH mice (Figures 4C-D). GLUT1-deficient cytotoxic T cells remain phenotypically and functionally unaffected [24], indicating that other glucose uptake mechanisms exist in cytotoxic T cells. GLUT1 and GLUT3 are essential for the activation and effector function of T cells [24, 25]. We revealed that intratumoral CD8$^+$ T cells massively upregulated GLUT3 but not GLUT1 (Figure S8A), and this finding was supported by single cell sequencing analysis (Figure S8B), suggesting the GLUT3-dependent glucose uptake in CD8$^+$ T cells.

Given the wide range of peripheral 5-HT actions, we hypothesized that citalopram modulates the immune system through the serotonergic mechanisms. Indeed, citalopram administered for 2 weeks in tumor-bearing mice led to reduced serum 5-HT levels (Figure 4E), which were accompanied with a reduction of low-grade systemic inflammatory responses in the MASH mice (Figure 4F). Compared to the control C57BL/6 mice, tumor-bearing *Tph1*$^{-/-}$

mice, which lack peripheral 5-HT, exhibited slowed tumor growth and increased effector function of intratumoral $CD8^+$ T cells (Figures 4G-I). Interestingly, citalopram reduced serum 5-HT to a level as observed in *Tph1*$^{-/-}$ mice, and displayed a superior inhibitory effect on tumor growth and $CD8^+$ T cell function compared with that induced by *Tph1* deficiency (Figures 4G-I). This finding suggests a dual immunostimulatory roles of citalopram on $CD8^+$ T cells, particularly the serotonergic-dependent mechanism. Next, we investigated the direct effects of citalopram on T cell activation, expansion, and cytotoxicity. Citalopram enhanced αCD3/αCD28-stimulated $CD8^+$ T cell proliferation as indicated by CFSE staining (Figure S9A). Moreover, citalopram promoted the TCR-instigated activation of $CD8^+$ T cells and the generation of effector $CD8^+$ T cells as evidenced by the cell surface expression of CD44 and CD62L (Figure S9B). Likewise, the cytotoxic activity of activated $CD8^+$ T was enhanced by citalopram, as reflected by GZMB, IFNγ, and TNF-α staining (Figures S9C-E).

Finally, to examine the immune-dependent anti-tumor effects of citalopram, we depleted either $CD8^+$ or $CD4^+$ T cells from $GLUT1^{KD}$ Hepa1-6 tumor-bearing mice and found that depletion of $CD8^+$ T cells, rather than $CD4^+$ T cells, increased tumor growth in citalopram-treated mice but had marginal effects in control mice (Figure 4J), showing that $CD8^+$ T cells are needed in the effector mechanisms of citalopram.

Discussion

Repurposing approved non-oncology drugs for cancer therapy offers cost-effectiveness, an accelerated development timeline, and a known safety profile as key advantages. Accumulating studies have deciphered the inverse link between SSRIs use and cancer risk. However, there is a scarcity of studies investigating the potential repurposing SSRIs for cancer treatment and their mechanisms of action. Non-oncology drugs may have mechanisms of action that are different from traditional cancer treatments. Previously, we and others have uncovered several new targets of SSRIs, including GLUT1 in HCC, SMPD1 in glioblastoma [26], and VDAC1 in autophagy [27]. Here, we further broaden the knowledge of how SSRIs impact the immune system to exert anti-tumor effects. By targeting C5aR1 on TAMs, citalopram enhances the phagocytic activity of TAMs and boosts local anti-tumor immune responses. Furthermore, treatment with citalopram results in a reduction in circulating 5-HT

levels and this phenomenon is akin to the deficiency of *Tph1* and enhances the activation of $CD8^+$ T cells. Therefore, these insights shed light on the immunomodulatory role of SSRIs in the context of cancer treatment (Figure 5).

C5aR1 is expressed on TAMs within the TME, which helps to explain why citalopram has better anti-tumor effects in immune-competent mice. In addition to TAMs, C5aR1 is also expressed by neutrophils, mast cells, and myeloid-derived suppressor cells in cancers [14, 28, 29]. Although the functional impacts of citalopram on these C5aR1-expressing immune cells have not been formally determined, macrophage depletion assay and $C5aR1^{-/-}$ BMDM co-injection experiment suggested that citalopram exerted anti-tumor functions *in vivo* through C5aR1-expressing TAMs. $C5aR1^+$ macrophages are profoundly implicated in squamous carcinogenesis and targeting C5aR1 reprograms macrophages to recruit cytotoxic $CD8^+$ T cells [14]. In alignment with this, citalopram treatment increased $CD8^+$ T cell filtration and their cytotoxic activities in HCC, and this effect was largely dependent on $C5aR1^+$ macrophages. One possible explanation is that citalopram targets C5aR1 to enhance macrophage phagocytosis and subsequent antigen presentation and/or cytokine production, which promotes T cell recruitment and activity as well as modulate other aspects of tumor immunity. Moreover, citalopram induces TAM phenotypic polarization towards to a proinflammatory state, which supports anti-tumor immune response within the TME. Therefore, we provide a mechanistic insight regarding how citalopram target C5aR1 activity in TAMs, the central findings are important to our understanding of citalopram-induced anti-tumor activities and may lay a basis for upcoming mechanistic studies aimed to decipher specific tumor-promoting roles of this defined TAM population.

While we highlight the anti-HCC effects of SSRIs through targeting C5aR1, it is possible that SSRIs impact tumor progression by modulating the systemic environment via serotonergic mechanisms, especially concerning the activation of $CD8^+$ T cells. Apart from its role in regulating hemostasis, 5-HT exerts immunoregulatory functions on circulating immune cells [30]. In this study, it was observed that both citalopram treatment and *Tph1* deficiency enhanced $CD8^+$ T cell cytotoxic activity. Consistently, peripheral 5-HT has been shown to dampen the effector functions of $CD8^+$ T cells within tumors [31]. Similarly, treatment with SSRIs such as fluoxetine increased the influx of $CD8^+$ T cells and reduced the growth of syngeneic

pancreatic and colorectal tumors [31]. In addition to the traditional receptor-dependent signaling transduction, 5-HT can modulate $CD8^+$ T activity through post-translational modification known as serotonylation [32]. It remains to be explored whether serotonylation contributes to the immunomodulatory effects of citalopram, as citalopram directly stimulates CD8+ T cell proliferation, activation, and cytotoxicity *in vitro*. The observed reduction in serum 5-HT levels and activation of $CD8^+$ T cells following SSRI treatment further highlight the complex interplay between neurotransmitters, the immune system, and cancer progression. Immunotherapy, especially immune checkpoint inhibitors (ICIs), has revolutionized the management of HCC [33]. The immune microenvironments play crucial roles in the response or resistance of HCC to immunotherapies [34]. However, limited molecular biomarkers are available to guide clinical decision-making for ICI therapy of HCC. Given SSRIs can increase $CD8^+$ T cell infiltration as well as cytotoxic activities by targeting $C5aR1^+$ TAMs, one can suppose that $C5aR1^+$ TAMs within the HCC microenvironment might be used as a molecular marker for SSRIs use in combination with ICI therapy.

In conclusion, our study suggests the potential repurposing of SSRIs for the treatment of HCC and highlights C5aR1 as a direct target of citalopram. We elucidate the immune-dependent mechanisms of action of citalopram, involving the regulation of both TAMs and $CD8^+$ T cells. Combining SSRIs with ICIs or other first-line therapies could enhance the treatment efficacy of current standard therapies.

Materials and Methods

Animal models.

In the subcutaneous xenograft model, $Rag1^{-/-}$ C57BL/6N mice (male, 6-8-week-old, Cyagen Biosciences, C001197), wild type immune-competent C57BL/6 mice (male or female, 6-8-week-old) or *Tph1*$^{-/-}$ mice (male, 6-8-week-old, Cyagen Biosciences, S-KO-05541), were maintained on a 12-hour day/night cycle with ad libitum access to food and water. For the pharmacological inhibition study, 5×10^6 mouse HCC cells (wild type, shControl, sh*Slc6a4* or sh*Slc2a1* Hepa1-6 and Hep53.4) in 100 μl HBS were injected subcutaneously in the lower back. When bore visible tumors, mice were given intraperitoneal injections of vehicle or citalopram (5 mg/kg body weight, Selleck, Shanghai, China) daily (n = 5-7 per group).

In the orthotopic xenograft model, 5 × 10^6 Hepa1-6 cells transfected with luciferase-expressing lentiviruses were orthotopically implanted into the liver of WT or MASH C57BL/6 mice. The day following tumor cell implantation, mice were treated with citalopram (5 mg/kg body weight) or DMSO. In the diet-induced MASH model, mice were fed a choline-deficient, amino acid-defined high-fat diet (45 kcal% fat) supplemented with 0.1% methionine (CDAHFD diet, A06071309, from Research Diets) for a duration of 6 weeks.

For the C5aR1 knockdown study, C57BL/6J-*C5ar1*^{em1Cya} mice were purchased from Cyagen Biosciences (S-KO-01274, Suzhou, China). 5 × 10^6 sh*Slc2a1* Hepa1-6 cells were injected into the lower back of 6-8-week-old male *C5ar1*$^{+/-}$ or *C5ar1*$^{-/-}$ C57BL/6 mice. Tumor volume was measured every week using a digital caliper. Four weeks later, mice were sacrificed and xenograft tumors were analyzed.

To determine the association between citalopram and C5aR1, 2 × 10^6 GLUT1^{KO} Hepa1-6 cells were mixed 1:1 with BMDMs (*C5ar1*$^{+/-}$ or *C5ar1*$^{-/-}$) in growth factor-reduced Matrigel (#354230, Corning, Shanghai, China) and injected into the lower back of 6-8-week-old male *C5ar1*$^{-/-}$ C57BL/6 mice. To acquire BMDMs, bone marrow was harvested from the femurs and tibias of *C5ar1*$^{+/-}$ or *C5ar1*$^{-/-}$ mice. Then, isolated cells were cultured in RPMI 1640 supplemented with 10% FBS, stimulated with recombinant CSF-1 (20 ng/ml, 416-ML, R&D systems), and maintained at 37°C in a humidified atmosphere with 5% CO_2. Differentiation of BMDMs was confirmed by flow cytometric analysis of F4/80 (28463-1-AP, Proteintech) and CD45 (20103-1-AP, Proteintech) expression. One week after cancer cell implantation, mice were subjected to treatment with citalopram (5 mg/kg body weight) or DMSO. At indicated time point, mice were sacrificed and xenograft tumors were analyzed.

In all animal studies, tumor volume was assessed using caliper measurements and calculated using the formula: tumor = 1/2(length × width$^{\wedge 2}$), where length represents the largest diameter and width indicates the smallest diameter. At the experimental endpoint, mice were humanely euthanized, tumors were excised, and tumor weight was recorded. All animals received proper care in accordance with the guidelines outlined in the “Guide for the Care and Use of Laboratory Animals” established by the National Academy of Sciences and published by the National Institutes of Health (NIH publication 86-23 revised 1985). The protocols for animal studies were approved by the ethics committee of the Ren Ji Hospital,

School of Medicine, Shanghai Jiao Tong University (approval number 202201427 and RA-2021-096).

Cell culture and reagents.

The following cell lines were included: Hepa1-6, Hep53.4, THP-1, and HEK293T. All cells were cultured in a medium recommended by ATCC, supplemented with 10% fetal bovine serum (FBS; Gibco, USA) and 1% (v/v) streptomycin-penicillin (Sigma-Aldrich, Shanghai, China), and maintained at 37°C in a humidified atmosphere with 5% CO_2. Prior to conducting cell experiments, all the mentioned cell lines underwent testing for short tandem repeat profiling and mycoplasma contamination to ensure their authenticity and purity. Citalopram (S4749), escitalopram (S4064), fluoxetine (S1333), fluvoxamine (S1336), paroxetine (S3005), and sertraline (S4053) were all obtained from Selleck (Shanghai, China).

Plate colony formation assay.

For cell proliferation analysis, a total of 1,000 indicated HCC cells were seeded into 6-well plates with three replicates. After treatment with citalopram for 10-14 days, the plates were washed with phosphate-buffered saline (PBS) twice, fixed with methanol for 10 min, and stained with 0.5% (w/v) crystal violet solution for 10 min. Colonies containing more than 30 cells were counted under the microscope.

Detection of Caspase-3/7 activity.

Cell apoptosis in HCC cells upon citalopram treatment was assessed using the Apo-ONE® Homogeneous Caspase-3/7 Assay (Promega, Madison, WI, USA) as described previously [35]. To normalize the data, the cell number in the same plate was detected using CellTiter-Blue (Promega, G8081). The relative Caspase-3/7 activity was determined by calculating the ratio of the signals obtained from the Apo-ONE assay to those from the CellTiter-Blue assay.

Gene knockdown and knockout.

The specific shRNA oligonucleotides targeting *Slc6a4* and *Slc2a1* were custom-synthesized

by Genepharma (Shanghai, China). Lentivirus packaging was carried out in HEK293T cells using Lipofectamine 2000 (Invitrogen, Carlsbad, CA), and virus titers were determined following standard procedures. HCC cells (Hep53.4 and Hepa1-6) were infected with the virus-containing supernatant in the presence of 6 μg/ml polybrene (Sigma-Aldrich, H9268, St. Louis, MO) when they reached 70% confluence. Cells expressing the shRNAs were selected using puromycin (2 μg/ml, Gibco, A1113802).

For CRISPR/Cas9-mediated gene knockout, THP-1 cells were initially transfected with the lentiCas9-Blast vector to facilitate the expression of Cas9. To generate *C5aR1*$^{-/-}$ THP-1 cells, a lentiviral system utilizing guide RNA (sgRNA) targeting C5AR1 was utilized. The lentivirus was produced in HEK293T cells by transfecting lentiGuide-Puro along with packaging plasmids pVSVg and psPAX2. The transfection was carried out using Fugene6 (E2693, Promega) in OptiMEM. After two days, the supernatants were filtered through a 0.45 μm filter, and Cas9-expressing cells were infected with the lentivirus in the presence of 6 μg/ml polybrene. Individual colonies were then seeded into 96-well plates, allowed to reach confluence, and subsequently subjected to knockout efficiency analysis. The sequences for shRNA and sgRNA are provided below: sh*Slc6a4*, CACCGCCTCCTACTATAACACCATCCGAAGATGGTGTTATAGTAGGAGGC; sh*Slc2a1*, CACCGGGAGAAGAAGGTCACCATCTCGAAAGATGGTGACCTTCTTCTCCC; *C5AR1* sgRNA, CTTCAGTCAACACGTTCCGG.

Quantitative real-time PCR (qRT-PCR).

RNA was extracted from CD8^{+} T cells using the RNAiso Plus reagent (Takara, Japan) and subjected to reverse transcription using the PrimeScript RT-PCR kit (Takara, Japan). Then, qRT-PCR was performed using the 7500 Real-time PCR system (Applied Biosystems, USA). The housekeeping gene *Gapdh* was used to normalize gene expression. Primer sequences used in this study were shown below: *Slc2a1* forward, 5'-CAGTTCGGCTATAACACTGGTG-3'; *Slc2a1* reverse, 5'-GCCCCCGACAGAGAAGATG-3'; *Slc2a3* forward, 5'-ATGGGGACAACGAAGGTGAC-3'; *Slc2a3* reverse, 5'-GTCTCAGGTGCATTGATGACTC-3'; *Gapdh* forward, 5'-AGGTCGGTGTGAACGGATTTG-3'; *Gapdh* reverse, 5'-TGTAGACCATGTAGTTGAGGTCA-3'.

Immunoblotting.

Cellular lysates were extracted using RIPA lysis buffer (P0013B, Beyotime, Shanghai, China) supplemented with protease and phosphatase inhibitor cocktails (ab201119, Abcam, Shanghai, China). The protein concentration was quantified with a BCA Protein Assay Kit (Pierce Biotechnology, USA). The proteins were then separated by sodium dodecyl sulfate-polyacrylamide gel electrophoresis (SDS-PAGE) and transferred onto polyvinylidene difluoride (PVDF, Millipore) membranes. Subsequently, the membranes were blocked with 5% (m/v) skim milk for 1 h at room temperature before being incubated with specific antibodies overnight at 4°C. On the following day, the membranes were washed three times with PBS and then incubated with HRP-conjugated secondary antibodies for 45 min. Subsequently, an ECL chemiluminescence assay (SB-WB012, Share-bio, Shanghai, China) was performed using a Bio-Spectrum Gel Imaging System (Bio-Rad). The antibodies utilized in this study included: SERT (1:500, ProteinTech, 19559-1-AP), GLUT1 (1:2,000, Cell Signaling Technology, #73015), C5aR1 (1:1,500, ProteinTech, 21316-1-AP), and β-actin (1:2,000, Abcam, ab8226). The information for secondary antibodies is as follows: goat anti-rabbit IgG (H+L) cross-adsorbed secondary antibody (1:5,000, Thermo Fisher Scientific, G-21234) and goat anti-mouse IgG (H+L) cross-adsorbed secondary antibody (1:5,000, Thermo Fisher Scientific, G-21040).

Immunohistochemistry and immunofluorescence analysis.

Paraffin-embedded sections of mouse HCC tissues were subjected to immunohistochemical analysis of Ki67, cleaved caspase 3, and C5aR1 expression. Immunohistochemical analysis was performed as reported previously [35]. The primary antibodies used in this study were shown as follows: Ki67 (1:400, Cell Signaling Technology, #9449), cleaved caspase 3 (1:400, Cell Signaling Technology, #9661), and C5aR1 (1:1,200, ProteinTech, 21316-1-AP). For immunofluorescence analysis, paraffin sections (5 μm) of HCC samples were deparaffinized and rehydrated with graded ethanol, followed by microwave heating-based antigen retrieval. Then tissue sections were blocked with 10% donkey serum (Sigma-Aldrich, D9663, USA) for 1 h at room temperature and incubated with primary antibodies at 4°C overnight. The

following antibodies were used: C5aR1 (1:50, Proteintech, 10375-1-AP) and CD163 (1:200, Abcam, ab182422). The next day, tissue sections were incubated with donkey anti-rabbit Alexa Fluor 594 (1:400, Jackson ImmunoResearch, #711-585-152) and donkey anti-mouse Alexa Fluor 488 (1:400, Jackson ImmunoResearch, #715-545-150) for 30 min at room temperature. Finally, 4',6-diamidino-2-phenylindole (DAPI) staining was performed to visualize the nuclei. Confocal microscope equipped with a digital camera (Nikon, Japan) was used for high-resolution imaging.

Bioinformatics analysis and single cell sequencing data.

Correlation analysis was performed with GEPIA2 (http://gepia2.cancer-pku.cn/#index) [36]. The following gene signatures were included for analysis, TAMs (*CD33*, *MARCO*, *CXCL5*, *SULT1C2*, *MSR1*, *CTSK*, *PTGDS*, *COLEC12*, *GPC4*, *PCOLCE2*, *CHIT1*, *CLEC5A*, *CCL7*, *FN1*, *CD163*, *GM2A*, *BCAT1*, *RAI14*, *COL8A2*, *CHI3L1*, *ATG7*, *CD84*, *MS4A4A*, *EMP1*, *CYBB*, *CD68*, and *CD11b*), exhausted T cells (*HAVCR2*, *TIGIT*, *LAG3*, *PDCD1*, *CXCL13* and *LAYN*), immune checkpoint (*IDO1*, *IDO2*, *PDCD1*, *CD274*, *PDCD1LG2*, *CTLA4*, *LAG3*, *HAVCR2*, *C10orf54*, *BTLA*, *ICOS*, and *TNFRSF9*), and effector Treg cells (*FOXP3*, *CTLA4*, *CCR8*, and *TNFRSF9*). The single-cell transcriptome expression of C5aR1 and GLUT family members in the tumor microenvironment was identified with GSE125449 and GSE140228-10X.

DARTS experiments.

THP-1 or HEK293T cells were lysed using NP40 lysis buffer (Thermo Fisher Scientific, 89842Y). Following centrifugation at 12,000 rpm for 10 min, the supernatant containing the proteins was collected, and the protein concentration was determined using a BCA Protein Assay Kit (Pierce Biotechnology, USA). Samples of equivalent quality were then treated with specific SSRIs and a vehicle at 37°C for 4 h. Subsequently, pronase (10 μg/mL, Roche, 10165921001) or distilled water was added and incubated at room temperature for specified time points (10 and 30 min). The reaction was terminated by adding protease inhibitors, and the resulting products were harvested and subjected to analysis using Western blotting.

***In Silico* docking study.**

To predict the binding mode of citalopram/C5aR1, molecular docking was performed using the AutoDock 4.2.6 software package [37]. The receptor structure for C5aR1 (PDB id: 6C1Q) [20] was sourced from the RCSB protein data bank (https://www.rcsb.org/). Due to the lack of available structural information, the structure of mouse C5aR1 was predicted using a local version of the ColabFold (AlphaFold2) software [38, 39]. The original substrates and other heteroatoms in these crystal structures were removed for further docking procedure. The absolute structure of citalopram (CID: 2771), fluoxetine (CID: 3386), fluvoxamine (CID: 5324346), paroxetine (CID: 43815), and sertraline (CID: 68617) were sourced from the PubChem database (https://pubchem.ncbi.nlm.nih.gov/). In each docking scenario, molecular docking was conducted following a standard protocol [40], with a modification in the number of genetic algorithm runs to 500 to comprehensively explore the binding modes. The binding energy and cluster information were directly extracted from the AutoDock output.

Biochemical analysis.

The serum levels of inflammatory cytokines (TNF-α, IL-1β, and IL-6) were analyzed using commercial ELISA kits following the manufacturer's instructions (R&D Systems). The cytokine concentrations were calculated using a standard curve, and the data were presented in picograms per milliliter. Serum 5-HT levels were assessed using the 5-HT ELISA Kit from Abcam (ab133053), following the manufacturer's guidelines.

Isolation of TAMs from xenograft tumor tissues.

Fresh sterile tumor tissues from subcutaneous xenograft model were washed with PBS two times, minced with scalpels, and then digested using a Tumor Dissociation Kit (Miltenyi Biotec, cat #130-095-929) at room temperature for 30 min. Digested tumor tissues were filtered through Falcon 70Micrometer Cell Strainer (Corning, #352350) and centrifuged at 1,500 rpm for 5 min. Red blood cells were removed using Red Blood Cell Lysis Solution (Miltenyi Biotec, cat #130-094-183). Then, TAMs were selected by CD11b microbeads (Miltenyi Biotec, cat #130-049- 601) according to the manufacturer's instructions.

Isolation of immune cells and flow cytometry.

Mice were euthanized, and fresh tumor tissues and spleen were harvested. Spleens were mechanically disrupted through 70 μm Nylon mesh (Corning, #352350) to release single cells. The cells were washed with PBS, followed by the lysis of red blood cells with Red Blood Cell Lysis Solution (Miltenyi Biotec, cat #130-094-183). Tumor tissues were cut into small pieces with surgical scissors and digested with 2 mg/mL collagenase IV (Sigma) for 20 min and filtered with 70 μm Nylon mesh. The isolated cells were collected with PBS and subjected to centrifuged at 1,500 rpm for 5 min. To enrich immunocytes from tumor tissues, harvested cells were centrifuged through different concentrations of discontinuous gradients of 40/80 Percoll (GE Healthcare, cat #17-0891-01) at 350 × g for 30 min. The middle pellet was washed with PBS, subjected to red blood cell lysis for 3 min.

For staining molecules expressed on cell surface, single cell suspensions from spleens and tumor tissues were labeled with fluorophore-conjugated antibodies: PerCP-Cyanine 5.5 7AAD (Biolegend, Cat #420404, 1:1,000), FITC anti-mouse CD4 (Biolegend, Cat #100406, 1:1,000), PE anti-mouse Ly6G (Biolegend, Cat #127608, 1:200), APC anti-mouse CD11c antibody (Biolegend, Cat #117310, 1:200), PE-cy7 anti-mouse CD8α (Biolegend, Cat #100722, 1:200), Brilliant Violet 421 anti-mouse CD3 (Biolegend, Cat #100227, 1:200), Alex Fluor 647 anti-mouse F4/80 (Invitrogen, Cat #2604384, 1:200), Brilliant Violet 510 anti-mouse CD45 (Biolegend, Cat #103138, 1:200), PE-cy7 anti-mouse NK1.1 (Biolegend, Cat #156513, 1:200), Brilliant Violet 421 anti-mouse B220 (Biolegend, Cat #103240, 1:200), Brilliant Violet 605 anti-mouse CD11b (Biolegend, Cat #101257, 1:200), APC-CY7 Stain 780 (BD Bioscience, Cat #565388, 1:1,000).

For intracellular staining, single cell suspensions from tumor tissues were stimulated with Cell Stimulation Cocktail (Invitrogen) for 4 h, and labeled with PE anti-mouse CD45 antibody (Biolegend, Cat #103106, 1:200), PerCP-Cyanine 5.5 CD3 (Biolegend, Cat #100325, 1:200), PE-cy7 anti-mouse CD8a (Biolegend, Cat# 100722, 1:200), APC-CY7 Stain 780 (BD Bioscience, Cat #565388, 1:1,000). After fixation and permeabilization using the Fix/Perm kit (ThermoFisher, GAS004), cells were labeled with APC anti-human/mouse Granzyme B Recombinant antibody (Biolegend, Catalog no.372203, 1:200), Brilliant Violet 421 anti-mouse IFN-γ (Biolegend, Cat #505830, 1:200), Brilliant Violet 605 anti-mouse TNF-α (Biolegend, Cat

#506329, 1:200). Flow cytometry was performed in BD FACSCanto II.

T cell activation, expansion and cytotoxicity

Single-cell suspensions were freshly dissected from the spleen and lymph nodes, and red blood cells were removed using Red Blood Cell Lysis Solution (Miltenyi Biotec, cat #130-094-183). $CD8^+$ T cells were isolated from the resulting cell suspensions by $CD8^+$ magnetic bead selection (Miltenyi Biotec, cat #130-117-044). For T cell proliferation assay, isolated $CD8^+$ T cells were resuspended in PBS supplemented with carboxy fluorescein succinimidyl ester (CFSE, Invitrogen, 1:10,000) for 8 min at room temperature and washed with RPMI 1640, supplemented with 10% heat-inactivated FBS. Then, $CD8^+$ T cells were activated by plate-bound αCD3ε (5 μg/mL, Biolegend, Catalog no.100359) and α-CD28 (2 μg/mL, Biolegend, Catalog no.102121) in complete RPMI 1640 medium at 37°C and 5% CO_2 for 72 h in the presence or absence of 5 μM citalopram treatment. Finally, cell proliferation was assessed by flow cytometry. For assessment of cellular activation and cytotoxicity, $CD8^+$ T cells were stimulated by Leukocyte Activation Cocktail (GolgiPlug™ BD, Catalog no.550583) for 4 h, resuspended in PBS/2% FBS containing PE anti-mouse CD62L antibody (Biolegend, Catalog no.104407, 1:200) and Brilliant Violet 510 anti-mouse/human CD44 Antibody (Biolegend, Catalog no.103044, 1:200), followed by incubation at room temperature for 30 min and washed in PBS/2% FBS. After fixation and permeabilization using the Cytofix/Cytoperm solution (BD Biosciences) for 20 min at 4°C, Brilliant Violet 421 anti-mouse IFN-γ antibody (Biolegend, Catalog no.505830, 1:200), APC anti-human/mouse Granzyme B Recombinant antibody (Biolegend, Catalog no.372203, 1:200) and Alexa Fluor 488 anti-mouse TNF-α antibody (Biolegend, Catalog no. 506313, 1:200) were employed for intracellular staining. Then, cell activation and cytotoxicity were assessed by flow cytometry.

Macrophage phagocytosis assay

Phagocytosis assays of tumor cells were performed as previously described [41]. Briefly, 5×10^4 phorbol myristate acetate (PMA, 100 ng/ml) primed THP-1 cells and harvested TAMs were seeded overnight in a 24-well tissue culture plate. The next day, HCC-LM3 cells and Hepa1-6 cells were labelled with pHrodo™ Green (Thermo, Cat #P35373, 1:1,000). After

incubating macrophages in serum-free medium for 2 h, the macrophages were labeled with CellTracker™ Deep Red Dye (Thermo, Cat #C34565, 6 ng/mL). Then, 5×10^4 predyed tumor cells were added to the macrophages, in the presence or absence of C5a stimulation and different SSRIs (5 μM). After incubation at 37 °C for 4 h, macrophages were extensively washed and imaged with Confocal Laser Scanning Microscope (Leica).

Macrophage depletion assay

The method for eliminating macrophages was reported previously [42]. Briefly, C57BL/6 mice were intraperitoneally injected with clodronate liposomes (1.4 mg/20 g body weight) to remove macrophages. Clodronate liposomes (Yeasen, 40337ES10, Shanghai, China) were given every three days for 12 days before tumor inoculation. After inoculation of sh*Slc2a1* ($GLUT1^{KD}$) Hepa1-6 cells, clodronate liposomes were also administered every three days until the end of the experiment. When the mice were sacrificed, liver and tumor tissues were extracted, and F4/80 staining (1:250, Cell Signaling Technology, #70076) was performed to determine the efficiency of macrophage deletion.

$CD4^+$ T cell and $CD8^+$ T cell depletion experiments

For $CD4^+$ T and $CD8^+$ T cell depletion, mice were treated intraperitoneally with 200 μg of specific monoclonal antibodies (Ultra-LEAF™ Purified anti-mouse CD8a Antibody, Biolegend, cat #100763; and Ultra-LEAF™ Purified anti-mouse CD4 Antibody, Biolegend, cat #100457) the day before the implantation of cancer cells and then with 100 μg twice a week for the entire duration of the experiment.

Statistical analysis.

The sample sizes for in vitro and in vivo studies determined based on similar studies in the field and through pilot studies. Details regarding sample sizes and biological replicates can be found in the figure legends. Continuous variables are presented as means ± SD. For comparisons between two independent groups, a two-tailed Student's t-test was employed. Statistical analyses involving more than two groups were conducted using either a one-way

analysis of variance (ANOVA) with Tukey's method or two-way ANOVA with Dunnett multiple comparisons, as specified. GraphPad Prism 9 (GraphPad Software Inc., San Diego, CA) was used for statistical analyses. Kaplan-Meier survival curves were generated and analyzed using the log-rank test. A p-value less than 0.05 was considered statistically significant. In all figures, statistical significance is represented as follows: *$p < 0.05$; **$p < 0.01$; ***$p < 0.001$.

ACKNOWLEDGMENTS

The research was supported by grants from National Natural Science Foundation of China (82001469 and 82071581), Shanghai Pilot Program for Basic Research- Shanghai Jiao Tong University (21TQ1400225), Natural Science Foundation of Shanghai (22ZR1459500), "Rising Stars of Medical Talents" Youth Development Program (Youth Medical Talents-Specialist Program), Clinical Medicine Research Center Construction Project of Huadong Hospital (LCZX2202), Shanghai Outstanding Young Medical Personnel Training Program & Excellence Project of Shanghai Municipal Health Commission (20224Z0009), and Key specialized diseases construction of Huadong Hospital (ZDZB2225).

AUTHOR CONTRIBUTIONS

Conceptualization: S.H.J.; Methodology: F.D., S.H.J., K.S., S.Z., L.J.J. and J.J.; Formal Analysis: F.D., S.H.J., S.Z. and L.J.J.; Resources: M.X.F., X. W. and S.H.J.; Investigation: all authors; Supervision: S.H.J., X. W. and Z.G.Z.; Funding Acquisition: S.H.J., Z.G.Z., Z.B. and F.D.; Writing-Original Draft: F.D., K.S., S.Z., L.J.J. and S.H.J; Writing-Review & Editing: all authors.

DECLARATION OF INTERESTS

The authors declare no conflicts of interest.

References

1. Pushpakom S, Iorio F, Eyers PA, et al. Drug repurposing: progress, challenges and recommendations. Nature Reviews Drug Discovery 2019;18:41-58.
2. Schipper LJ, Zeverijn LJ, Garnett MJ, et al. Can Drug Repurposing Accelerate Precision

Oncology? Cancer Discovery 2022;12:1634-1641.
3. Foretz M, Guigas B, Viollet B. Metformin: update on mechanisms of action and repurposing potential. Nature Reviews Endocrinology 2023;19:460-476.
4. Xia Y, Sun M, Huang H, et al. Drug repurposing for cancer therapy. Signal Transduction and Targeted Therapy 2024;9.
5. Fluyau D, Mitra P, Jain A, et al. Selective serotonin reuptake inhibitors in the treatment of depression, anxiety, and post-traumatic stress disorder in substance use disorders: a Bayesian meta-analysis. European Journal of Clinical Pharmacology 2022;78:931-942.
6. Singh I, Seth A, Billesbolle CB, et al. Structure-based discovery of conformationally selective inhibitors of the serotonin transporter. Cell 2023;186:2160-+.
7. Lee MJ, Huang CW, Chen YL, et al. Association between selective serotonin reuptake inhibitors and kidney cancer risk: A nationwide population-based cohort study. International Journal of Cancer 2021;148:1331-1337.
8. Fischer A, Rennert HS, Rennert G. Selective serotonin reuptake inhibitors associated with increased mortality risk in breast cancer patients in Northern Israel. International Journal of Epidemiology 2022;51:807-816.
9. Zhang NQ, Sundquist J, Sundquist K, et al. Combined Use of Aspirin and Selective Serotonin Reuptake Inhibitors Is Associated With Lower Risk of Colorectal Cancer: A Nested Case-Control Study. American Journal of Gastroenterology 2021;116:1313-1321.
10. Bhagavathula AS, Woolf B, Rahmani J, et al. Selective serotonin reuptake inhibitor use and the risk of hepatocellular carcinoma: a systematic review and dose-response analysis of cohort studies with one million participants. European Journal of Clinical Pharmacology 2022;78:547-555.
11. Carlson LE, Ismaila N, Addington EL, et al. Integrative Oncology Care of Symptoms of Anxiety and Depression in Adults With Cancer: Society for Integrative Oncology-ASCO Guideline. Journal of Clinical Oncology 2023;41:4562-+.
12. Lomenick B, Hao R, Jonai N, et al. Target identification using drug affinity responsive target stability (DARTS). Proceedings of the National Academy of Sciences of the United States of America 2009;106:21984-21989.
13. Beach C, MacLean D, Majorova D, et al. Improving radiotherapy in immunosuppressive microenvironments by targeting complement receptor C5aR1. Journal of Clinical Investigation 2023;133.
14. Medler TR, Murugan D, Horton W, et al. Complement C5a Fosters Squamous Carcinogenesis and Limits T Cell Response to Chemotherapy. Cancer Cell 2018;34:561-+.
15. Ajona D, Zandueta C, Corrales L, et al. Blockade of the Complement C5a/C5aR1 Axis Impairs Lung Cancer Bone Metastasis by CXCL16-mediated Effects. American Journal of Respiratory and Critical Care Medicine 2018;197:1164-1176.
16. Dong F, He K, Zhang S, et al. SSRI antidepressant citalopram reverses the Warburg effect to inhibit hepatocellular carcinoma by directly targeting GLUT1. bioRxiv 2024:2024.07.17.603851.
17. Pio R, Ajona D, Ortiz-Espinosa S, et al. Complementing the Cancer-Immunity Cycle. Frontiers in Immunology 2019;10.
18. Lomenick B, Hao R, Jonai N, et al. Target identification using drug affinity responsive target stability (DARTS). Proc Natl Acad Sci U S A 2009;106:21984-9.
19. Robertson N, Rappas M, Dore AS, et al. Structure of the complement C5a receptor bound to the extra-helical antagonist NDT9513727. Nature 2018;553:111-114.
20. Liu H, Kim HR, Deepak R, et al. Orthosteric and allosteric action of the C5a receptor antagonists. Nat Struct Mol Biol 2018;25:472-481.
21. Wang Y, Liu W, Xu Y, et al. Revealing the signaling of complement receptors C3aR and C5aR1 by anaphylatoxins. Nat Chem Biol 2023.
22. Eslam M, Newsome PN, Sarin SK, et al. A new definition for metabolic dysfunction-associated fatty liver disease: An international expert consensus statement. Journal of Hepatology 2020;73:202-209.
23. Du DY, Liu C, Qin MY, et al. Metabolic dysregulation and emerging therapeutical targets for hepatocellular carcinoma. Acta Pharmaceutica Sinica B 2022;12:558-580.
24. Macintyre AN, Gerriets VA, Nichols AG, et al. The Glucose Transporter Glut1 Is Selectively Essential for CD4 T Cell Activation and Effector Function. Cell Metabolism 2014;20:61-72.
25. Hochrein SM, Wu H, Eckstein M, et al. The glucose transporter GLUT3 controls T helper 17 cell responses through glycolytic-epigenetic reprogramming. Cell Metabolism 2022;34:516-+.
26. Bi JF, Khan A, Tang J, et al. Targeting glioblastoma signaling and metabolism with a re-

purposed brain-penetrant drug. Cell Reports 2021;37.
27. Hwang HY, Shim JS, Kim D, et al. Antidepressant drug sertraline modulates AMPK-MTOR signaling-mediated autophagy via targeting mitochondrial VDAC1 protein. Autophagy 2021;17:2783-2799.
28. Ou B, Liu Y, Yang X, et al. C5aR1-positive neutrophils promote breast cancer glycolysis through WTAP-dependent m6A methylation of ENO1. Cell Death Dis 2021;12:737.
29. Ding P, Li L, Li L, et al. C5aR1 is a master regulator in Colorectal Tumorigenesis via Immune modulation. Theranostics 2020;10:8619-8632.
30. Costa LHA, Santos BM, Branco LGS. Can selective serotonin reuptake inhibitors have a neuroprotective effect during COVID-19? European Journal of Pharmacology 2020;889.
31. Schneider MA, Heeb L, Beffinger MM, et al. Attenuation of peripheral serotonin inhibits tumor growth and enhances immune checkpoint blockade therapy in murine tumor models. Science Translational Medicine 2021;13.
32. Wang X, Fu SQ, Yuan X, et al. A GAPDH serotonylation system couples CD8+T cell glycolytic metabolism to antitumor immunity. Molecular Cell 2024;84.
33. Zheng Y, Wang S, Cai J, et al. The progress of immune checkpoint therapy in primary liver cancer. Biochim Biophys Acta Rev Cancer 2021;1876:188638.
34. Llovet JM, Castet F, Heikenwalder M, et al. Immunotherapies for hepatocellular carcinoma. Nat Rev Clin Oncol 2022;19:151-172.
35. Jiang SH, Li J, Dong FY, et al. Increased Serotonin Signaling Contributes to the Warburg Effect in Pancreatic Tumor Cells Under Metabolic Stress and Promotes Growth of Pancreatic Tumors in Mice. Gastroenterology 2017;153:277-291 e19.
36. Tang Z, Kang B, Li C, et al. GEPIA2: an enhanced web server for large-scale expression profiling and interactive analysis. Nucleic Acids Res 2019;47:W556-W560.
37. Morris GM, Huey R, Lindstrom W, et al. AutoDock4 and AutoDockTools4: Automated docking with selective receptor flexibility. J Comput Chem 2009;30:2785-91.
38. Mirdita M, Schutze K, Moriwaki Y, et al. ColabFold: making protein folding accessible to all. Nature Methods 2022;19:679-+.
39. Jumper J, Evans R, Pritzel A, et al. Highly accurate protein structure prediction with AlphaFold. Nature 2021;596:583-+.
40. Forli S, Huey R, Pique ME, et al. Computational protein-ligand docking and virtual drug screening with the AutoDock suite. Nat Protoc 2016;11:905-19.
41. Chen J, Zhong MC, Guo HJ, et al. SLAMF7 is critical for phagocytosis of haematopoietic tumour cells via Mac-1 integrin. Nature 2017;544:493-+.
42. Jiang SH, Zhu LL, Zhang M, et al. GABRP regulates chemokine signalling, macrophage recruitment and tumour progression in pancreatic cancer through tuning KCNN4-mediated Ca(2+) signalling in a GABA-independent manner. Gut 2019;68:1994-2006.

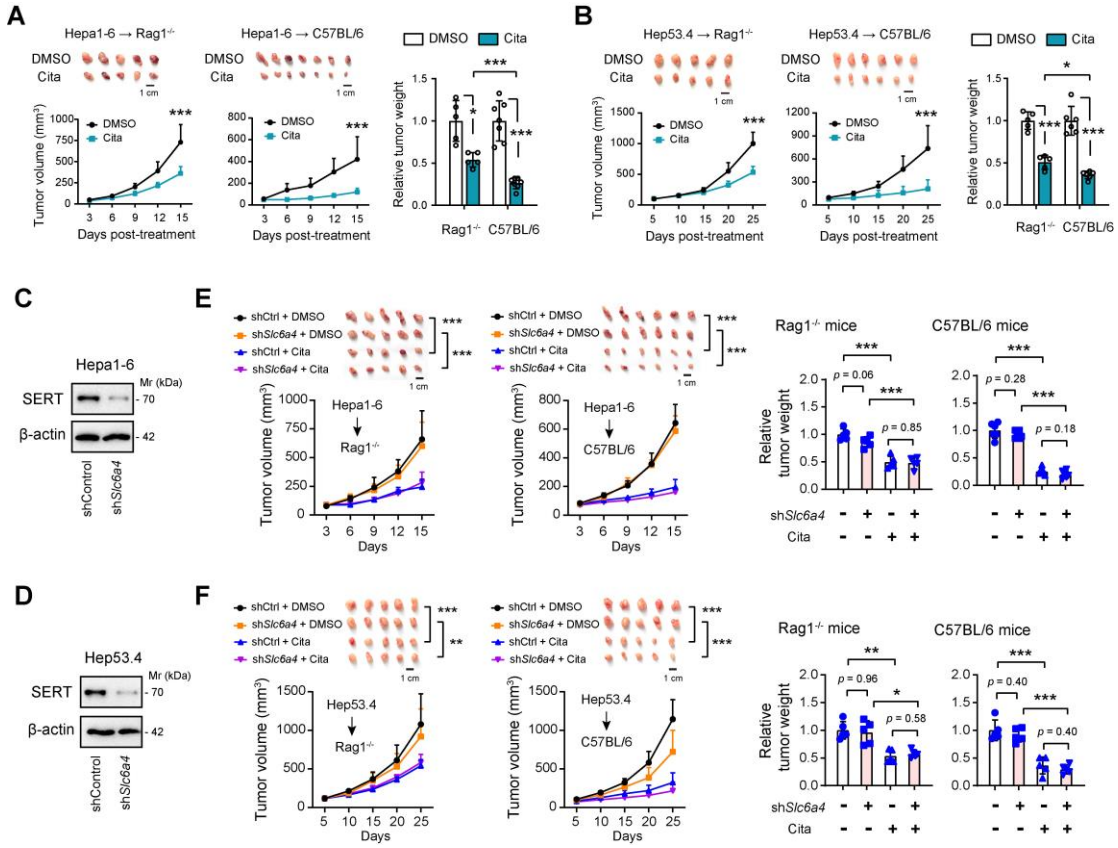

Fig. 1. The immune-dependent and SERT-independent anti-tumor effects of citalopram in HCC. (**A**, **B**) Mouse HCC cells, Hepa1-6 or Hep53.4, were subcutaneously injected into Rag1$^{-/-}$ C57BL/6 or immunocompetent C57BL/6 mice (n = 5-7 per group). When bore visible tumors, 5 mg/kg citalopram was treated daily for 15 or 25 days. Tumors were excised after mice were sacrificed, and the tumor weight was measured. (**C**, **D**) Western blotting showed the knockdown efficiency of SERT in Hepa1-6 and Hep53.4 cells. (**E**, **F**) shControl and sh*Slc6a4* Hepa1-6 and Hep53.4 cells were subcutaneously injected into Rag1$^{-/-}$ C57BL/6 or immunocompetent C57BL/6 mice (n = 5-6 per group). When bore visible tumors, 5 mg/kg citalopram was treated daily for 15 or 25 days. Tumors were excised after mice were sacrificed, and the tumor weight was measured. In all panels, *p < 0.05, **p < 0.01, ***p < 0.001. Values as mean ± SD and compared by one-way ANOVA multiple comparisons with Tukey's method (for bar chart comparison) and two-way ANOVA with Dunnett's multiple comparisons (for survival curve comparison).

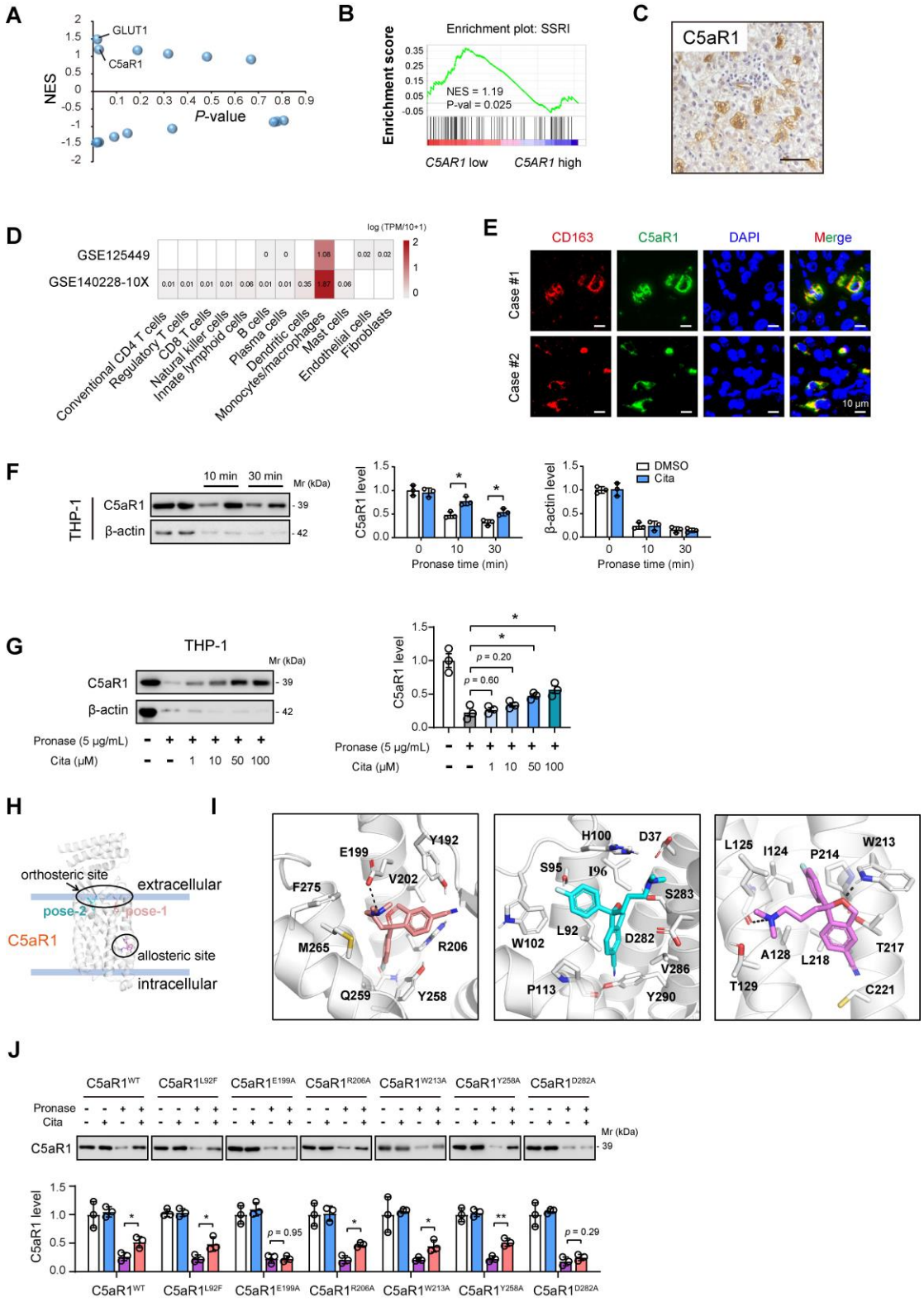

Fig. 2. C5aR1 is a direct target of citalopram.

(**A**) Gene Set Enrichment Analysis (GSEA) identified GLUT1 and C5aR1 as two top hits related to SSRI-induced gene changes. (**B**) GSEA of HCC RNAseq data (TCGA cohort) with the SSRI-related gene signature. Sample grouping was made based on the median

expression of C5aR1. (**C**) Representative immunohistochemical images showed the expression pattern and cellular distribution of C5aR1 in human HCC tissues. Scale bar, 50 μm. (**D**) Single cell RNA sequencing analysis showed the expression pattern of C5aR1 with the immune microenvironment of HCC. (**E**) Co-immunofluorescence of C5aR1 (green) with CD163 (red) in HCC samples. Scale bar, 10 μm. (**F**) The DARTS assay and immunoblot analysis showed C5aR1 protein stability against 5 μg/mL pronase in the presence and absence of 100 μM citalopram treatment. (**G**) The DARTS assay and immunoblot analysis showed C5aR1 protein stability against 5 μg/mL pronase in the presence of different concentration of citalopram treatment. (**H**) The overall conformation of citalopram binding to C5aR1. (**I**) Representative models of citalopram in pose-1 (left), pose-2 (middle) and allosteric site (right). Several polar interactions were indicated by black dashed lines. (**J**) HEK293T cells were transfected with either WT or mutant C5aR1 expression plasmids for 48 h, followed by DARTS assay with immunoblotting analysis of C5aR1 protein levels. In all panels, $^{*}p < 0.05$, $^{**}p < 0.01$. Values as mean ± SD and compared by the Student's t test (**F**) or one-way ANOVA multiple comparisons with Tukey's method among groups (**G**, **J**).

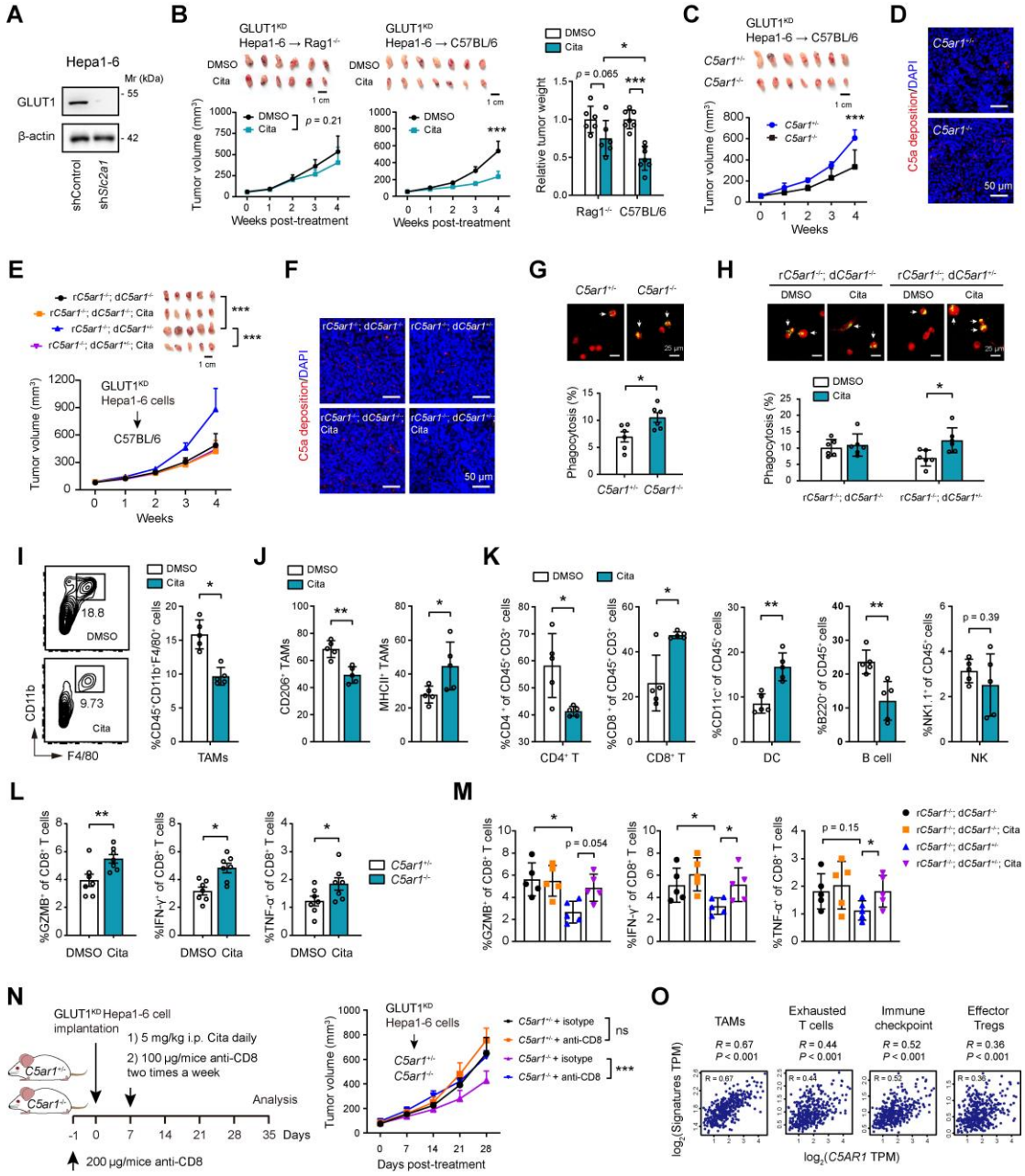

Fig. 3. Citalopram targets C5aR1^{+} TAMs

(**A**) Western blotting showed the knockdown efficiency of GLUT1 in mouse Hepa1-6 cells. (**B**) GLUT1^{KD} Hepa1-6 cells were subcutaneously injected into the Rag1$^{-/-}$ or immunocompetent C57BL/6 mice, and mice were treated with 5 mg/kg citalopram when bore visible tumors; three weeks later, tumor burden was examined (n = 6-7 per group). (**C**) The growth kinetics of GLUT1^{KD} Hepa1-6 tumors in *C5ar1*$^{+/-}$ and *C5ar1*$^{-/-}$ C57BL/6 host (n = 7). (**D**) Immunofluorescence analysis of C5a deposition in GLUT1^{KD} Hepa1-6 tumors from *C5ar1*$^{+/-}$ and *C5ar1*$^{-/-}$ C57BL/6 host. Scale bar, 50 μm. (**E, F, H**) GLUT1^{KD} Hepa1-6 cells admixed with *C5ar1*$^{+/-}$ and *C5ar1*$^{-/-}$ BMDMs from donor (d) mice were subcutaneously implanted into

syngeneic recipient (r) mice. The therapeutic effect of citalopram (**E**), C5a deposition (**F**), and macrophage phagocytosis (**H**) in this model were analyzed. Scale bar, 50 μm. (**G**) The phagocytic capacity of macrophages isolated from GLUT1^{KD} Hepa1-6 tumors in *C5ar1*$^{+/-}$ and *C5ar1*$^{-/-}$ C57BL/6 host. (**I-K**) Flow cytometry showed the infiltration of CD45^{+}CD11b^{+}F4/80^{+} macrophages (**I**), CD206^{+} TAMs and CD11b^{+} TAMs (**J**), tumor-infiltrating lymphocytes (**K**) in tumor tissues from orthotopic xenograft model, which generated in immunocompetent C57BL/6 mice with Hepa1-6 cells (n = 5 per group). (**L, M**) Measurement of CD8^{+} T cell function in tumor tissues from the groups mentioned in **C** and **E**. (**N**) The growth kinetics of GLUT1^{KD} Hepa1-6 tumors in *C5ar1*$^{+/-}$ and *C5ar1*$^{-/-}$ C57BL/6 host upon CD8^{+} T cell deletion (n = 7). (**O**) Correlation analysis of C5aR1 expression and immune checkpoint molecules, gene signatures of TAMs, exhausted T cells, and effector Tregs in the TCGA cohort (n = 371). In all panels, *$p < 0.05$, **$p < 0.01$, ***$p < 0.001$; ns, non-significant. Values as mean ± SD and compared by two-way ANOVA with Dunnett's multiple comparisons (**B**, **C**, **E**, **N**), Student's t test (**G**, **H**, **I-L**), one-way ANOVA multiple comparisons with Tukey's method (**B**, **M**), and the Spearman's rank correlation methods (**O**).

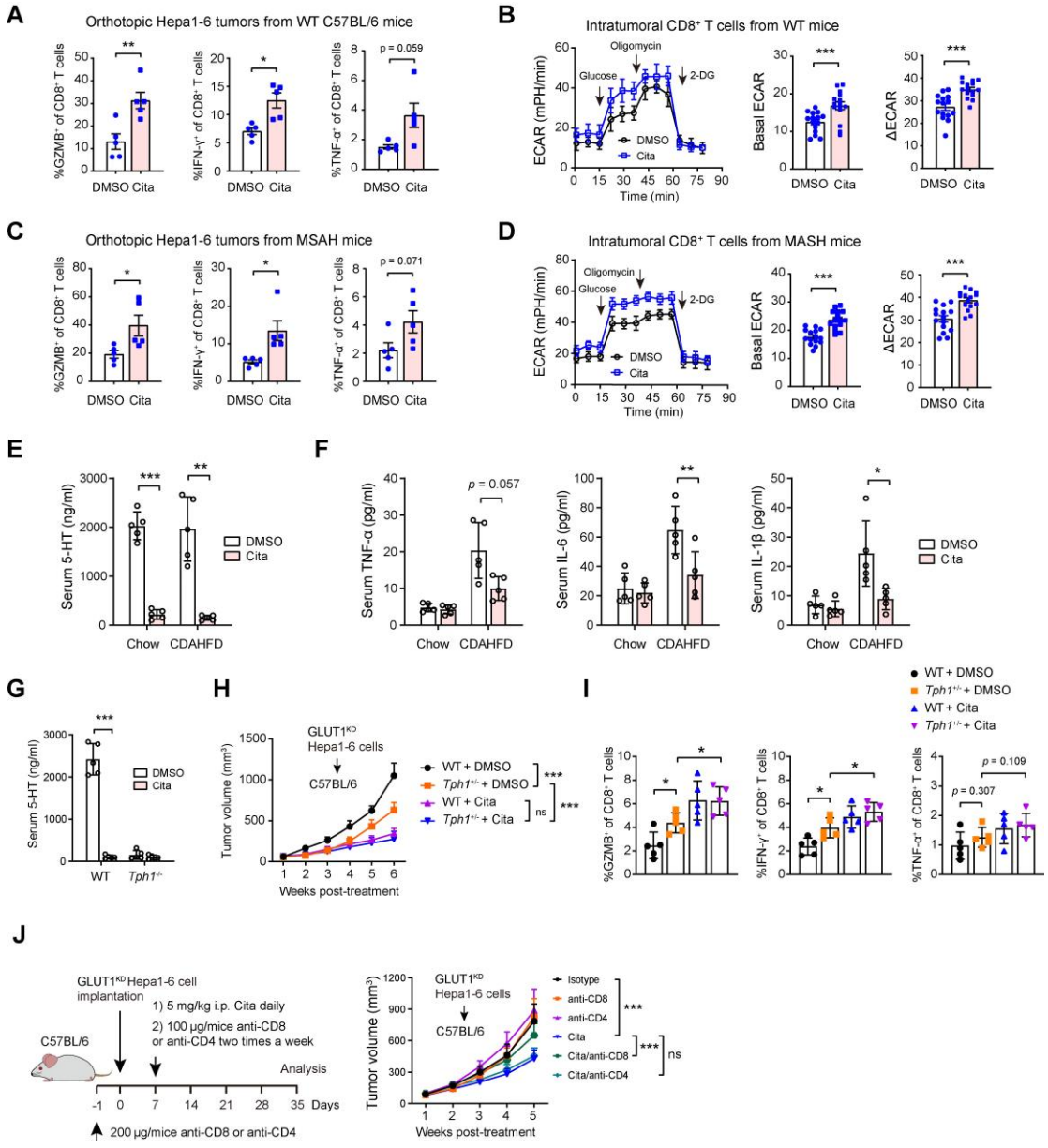

Fig. 4. Citalopram activates CD8$^+$ T cells.

(**A**, **B**) Measurement of CD8$^+$ T cell function and glycolysis in orthotopic tumor tissues from WT C57BL/6 mice (n = 5 per group). (**C**, **D**) Measurement of CD8$^+$ T cell function and glycolysis in orthotopic tumor tissues from MASH mice (n = 5 per group); Basal ECAR indicates glycolysis after the addition of glucose, and ΔECAR represents the difference between oligomycin-induced ECAR and 2-DG-induced ECAR. (**E**) Serum 5-HT levels in GLUT1^{KD} Hepa1-6 tumor-bearing mice fed with chow diet or CDAHFD, with the presence or absence of citalopram treatment (n = 5 per group). (**F**) Serum TNF-α, IL-1β, and IL-6 levels in GLUT1^{KD} Hepa1-6 tumor-bearing mice fed with chow diet or CDAHFD, with the presence or absence of citalopram treatment (n = 5 per group). (**G**) Serum 5-HT levels in WT C57BL/6

and *Tph1*$^{-/-}$ mice, with the presence or absence of citalopram treatment (n = 5 per group). (**H**) Tumor growth of WT and *Tph1*$^{-/-}$ mice after subcutaneous injection of Hepa1-6 cells and treatment with citalopram. (**I**) Measurement of CD8^{+} T cell function in tumor tissues from the groups mentioned in **H**. (**J**) The therapeutic effect of citalopram on GLUT1^{KD} Hepa1-6 tumor was tested in the presence or absence of CD4^{+} T or CD8^{+} T cell deletion. In all panels, *$p < 0.05$, **$p < 0.01$, ***$p < 0.001$; ns, non-significant. Values as mean ± SD and compared by the Student's t test (**A**-**F**), one-way ANOVA multiple comparisons with Tukey's method (**I**), and two-way ANOVA with Dunnett's multiple comparisons (**H**, **J**).

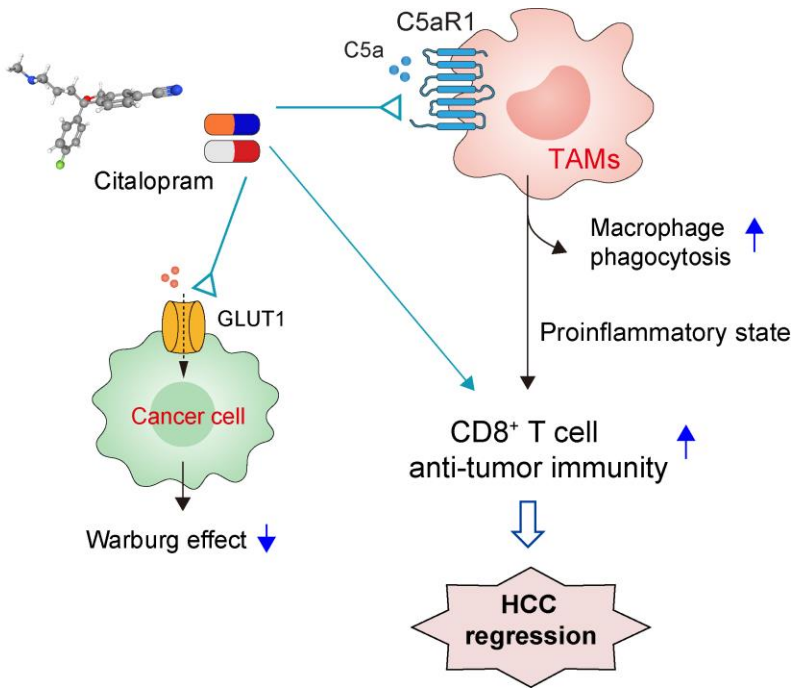

Fig. 5. Mechanism model.

Model depicting the molecular mechanism by which citalopram inhibit the Warburg effect and elicit an anti-tumor response in HCC. Citalopram not only inhibits glycolytic metabolism of cancer cells by targeting GLUT1 (Ref 16) but also enhances macrophage-driven anti-tumor immunity and induces a systemic immunostimulatory effect on $CD8^+$ T cell functions through serotonergic mechanisms.

Supplementary Materials

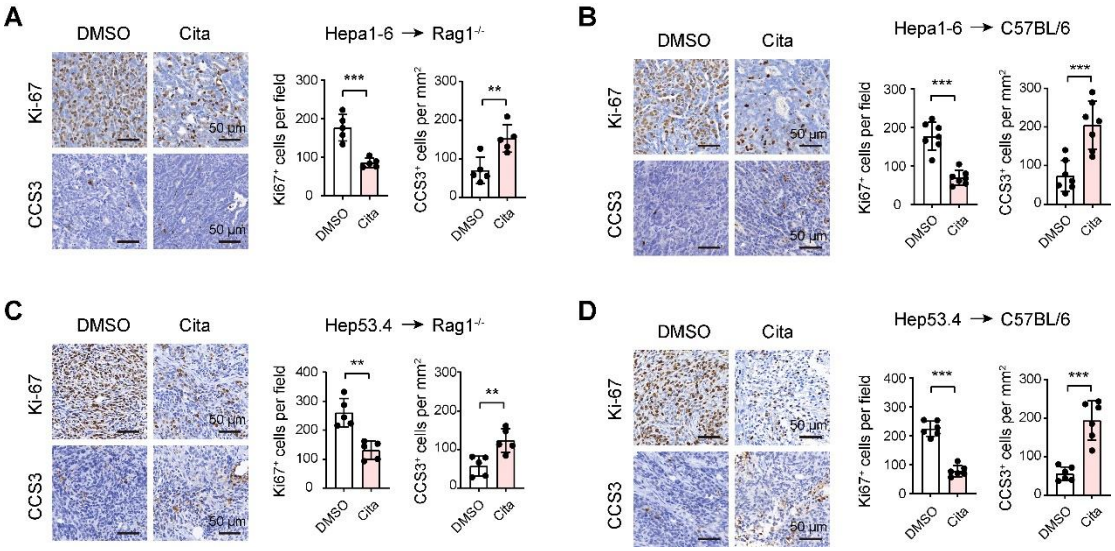

Figure S1. Citalopram inhibits HCC cell proliferation and promotes cell apoptosis in immune-competent and immune-deficient mouse models. (**A**, **B**) Immunohistochemical analysis of cleaved caspase-3 (CCS3) and Ki67 in Hepa1-6-bearing subcutaneous xenograft tumors from Rag1$^{-/-}$ or immunocompetent C57BL/6 mice, treated with DMSO or 5 mg/kg citalopram. (**C**, **D**) Immunohistochemical analysis of CCS3 and Ki67 in Hep53.4-bearing subcutaneous xenograft tumors from Rag1$^{-/-}$ or immunocompetent C57BL/6 mice, treated with DMSO or 5 mg/kg citalopram. In all panels, $^{**}p < 0.01$, $^{***}p < 0.001$. Scale bar, 50 μm. Values as mean ± SD and compared by the Student's t test.

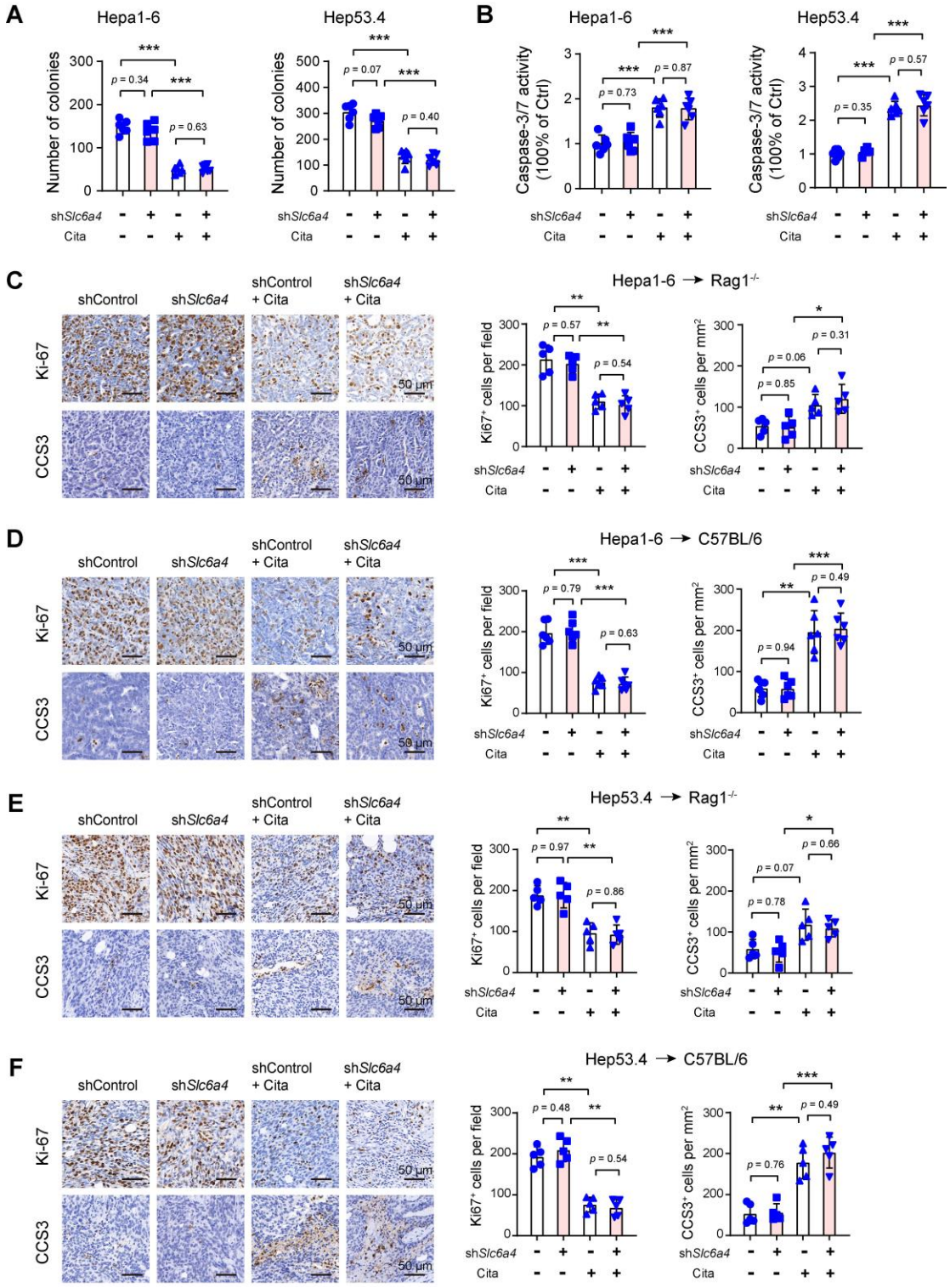

Figure S2. Citalopram suppresses HCC cell proliferation and promote cell apoptosis in a SERT-independent manner. (**A**) Plate colony formation assay revealed the effect of SERT knockdown alone or combined with citalopram treatment on the long-term cell proliferation of Hepa1-6 and Hep53.4 cells (n = 6 per group). (**B**) Caspase-3/7 activity in Hepa1-6 and Hep53.4 cells upon SERT knockdown or combined treatment with 5 μM citalopram (n = 6 per

group). (**C**, **D**) Immunohistochemical analysis of CCS3 and Ki67 in shControl and sh*Slc6a4* Hepa1-6-bearing subcutaneous xenograft tumors from Rag1$^{-/-}$ or immunocompetent C57BL/6 mice, treated with DMSO or 5 mg/kg citalopram. Scale bar, 50 μm. (**E**, **F**) Immunohistochemical analysis of CCS3 and Ki67 in shControl and sh*Slc6a4* Hep53.4-bearing subcutaneous xenograft tumors from Rag1$^{-/-}$ or immunocompetent C57BL/6 mice, treated with DMSO or 5 mg/kg citalopram. Scale bar, 50 μm. In all panels, *$p < 0.05$, **$p < 0.01$, ***$p < 0.001$. Scale bar, 50 μm. Values as mean ± SD and compared by one-way ANOVA multiple comparisons with Tukey's method among groups.

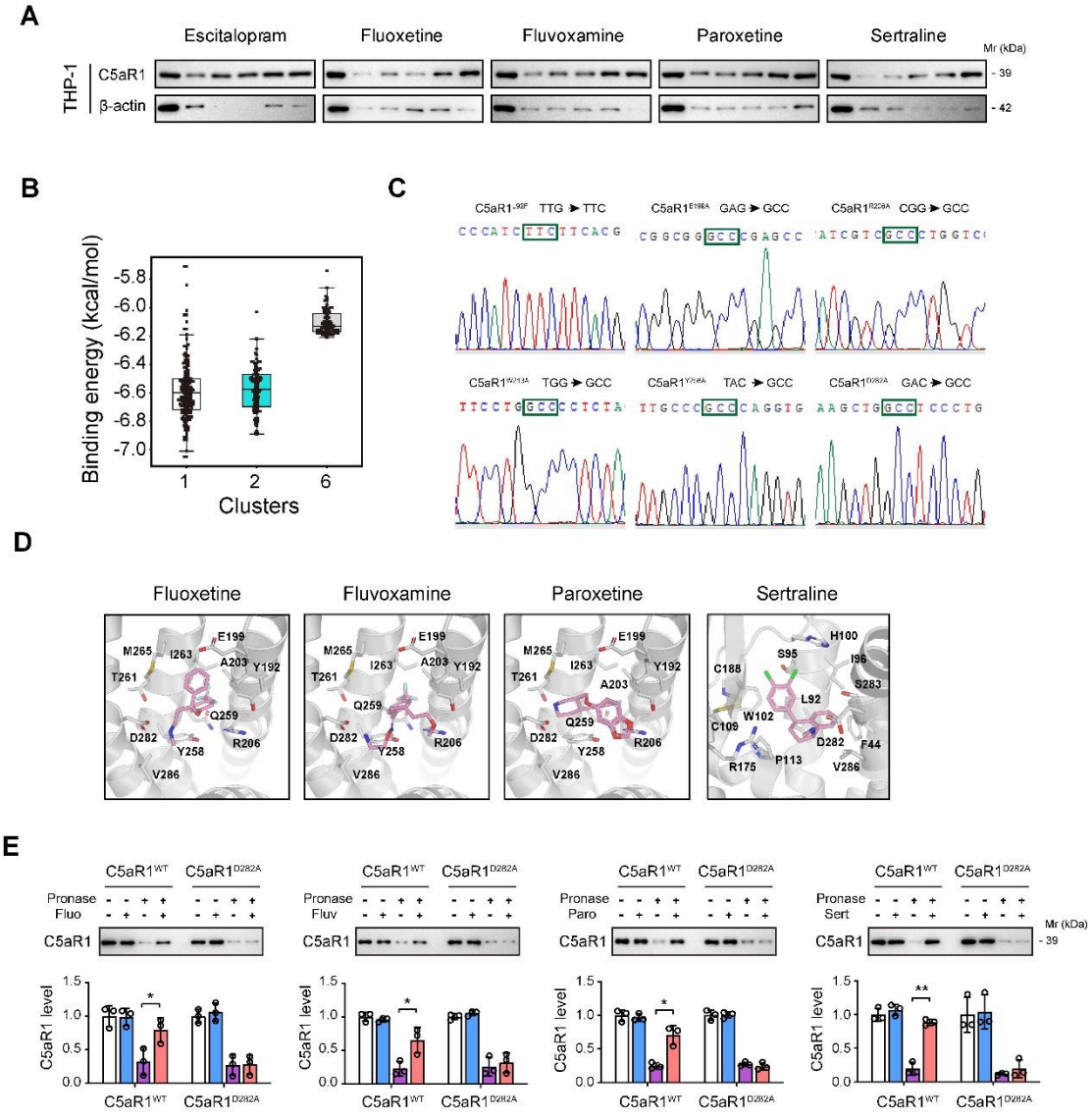

Figure S3. Identification of C5aR1 as a direct target for citalopram. (**A**) The DARTS assay and immunoblot analysis showed C5aR1 protein stability against 5 μg/mL pronase in the presence of different concentrations of SSRIs treatment (0, 1, 10, 50, and 100 μM). (**B**) For C5aR1, the predicted binding energy distribution of the clusters with poses more than 50. (**C**) Sequencing analysis showed the successful generation of six C5aR1 mutants. (**D**) The best-scored complex models of C5aR1 with other four different SSRIs. (**E**) HEK293T cells were transfected with either WT or mutant C5aR1 (D282A) expression plasmids for 48 h, followed by DARTS assay with immunoblotting analysis of C5aR1 protein levels. In all panels, *$p < 0.05$. Values as mean ± SD and compared by one-way ANOVA multiple comparisons with Tukey's method among groups (**E**).

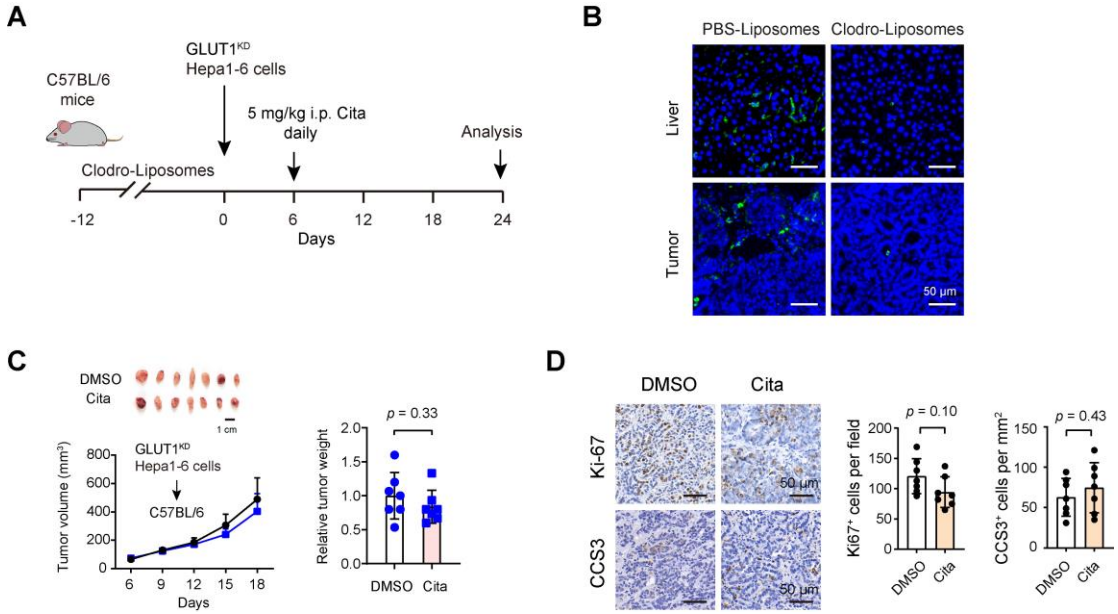

Figure S4. Macrophage depletion mitigates the anti-tumor effects of citalopram. (**A**) Schematic depicting macrophage blockade with clodronate liposomes. 12 days before tumor inoculation, C57BL/6 mice were pretreated with clodronate liposomes or phosphate-buffered saline (PBS) liposomes. Subsequently, GLUT1^{KD} Hepa1-6 cells were subcutaneously injected into the C57BL/6 mice. The effect of citalopram (5 mg/kg) on the tumor burden was evaluated after 18 days of drug treatment. (**B**) Immunofluorescence analysis of F4/80^{+} macrophages in the liver and tumor tissues of indicated groups. (**C**) In C57BL/6 mice, the effect of citalopram on the GLUT1^{KD} Hepa1-6 xenograft tumors was measured in the presence of macrophage deletion (n = 7 per group). (**D**) Immunohistochemical analysis of CCS3 and Ki67 in GLUT1^{KD} Hepa1-6-bearing subcutaneous xenograft tumors, treated with DMSO or 5 mg/kg citalopram (n = 7 per group). Scale bar, 50 μm. Values as mean ± SD and compared by the Student's t test (**C**, **D**) and two-way ANOVA with Dunnett's multiple comparisons (**C**).

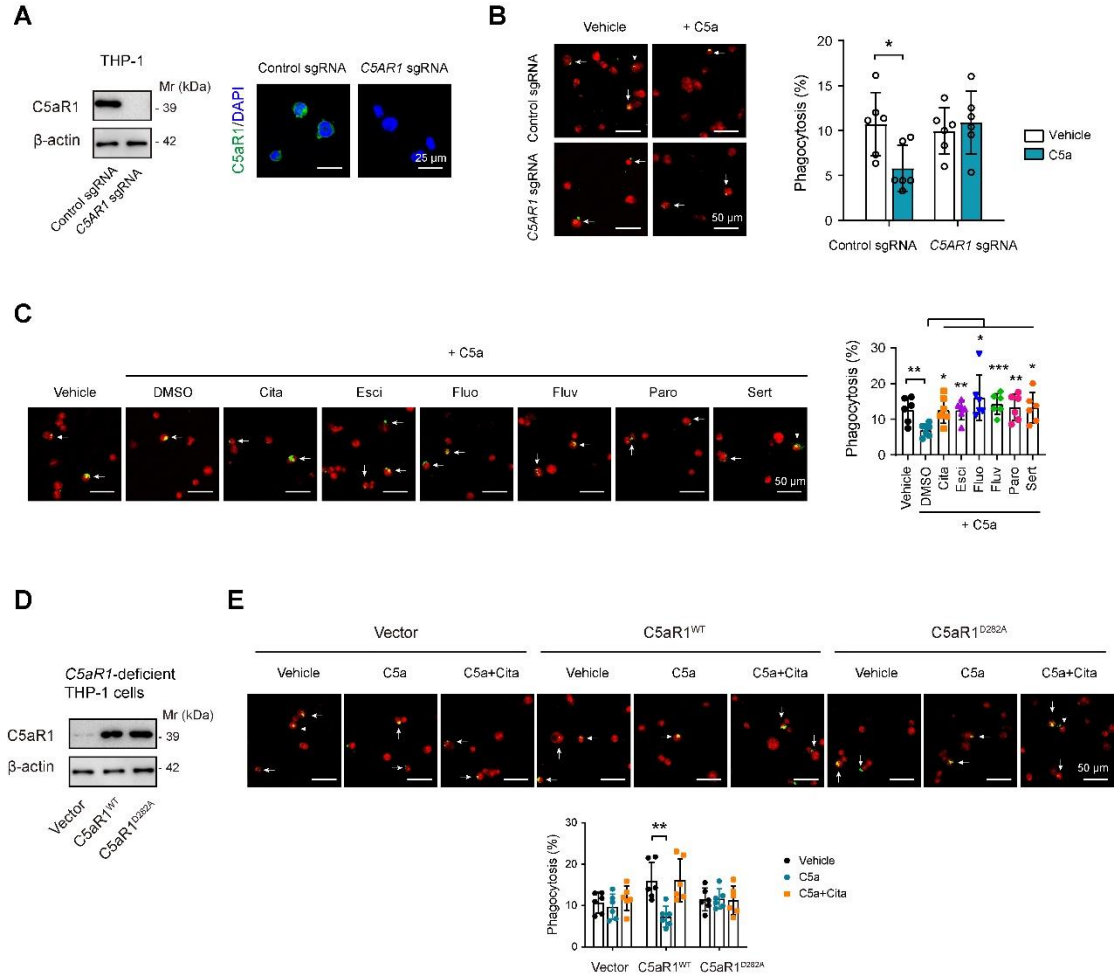

Figure S5. Citalopram reverses C5a-mediated macrophage phagocytic impairment via targeting C5aR1. (**A**) Western blotting and immunofluorescence analysis showed SERT protein levels in Cas9-sgControl, -sg*C5ar1* THP-1 subclones. (**B**) Effects of C5aR1 deficiency on the macrophage phagocytosis of HCC-LM3 in the presence or absence of C5a stimulation. (**C**) Effects of different SSRIs on the macrophage phagocytosis of HCC-LM3 in the presence of C5a stimulation. (**D**) Reconstituted expression of WT and D282A mutant C5aR1 in $C5aR1^{KO}$ THP-1 cells. (**E**) The effects of citalopram on macrophage phagocytosis in the absence of C5aR1 with reconstituted expression of $C5aR1^{WT}$ or $C5aR1^{D282A}$. In all panels, $*p < 0.05$, $**p < 0.01$, $***p < 0.001$. Values as mean ± SD and compared by one-way ANOVA multiple comparisons with Tukey's method among groups. Data are representative of three independent experiments (**B**, **C**, **E**).

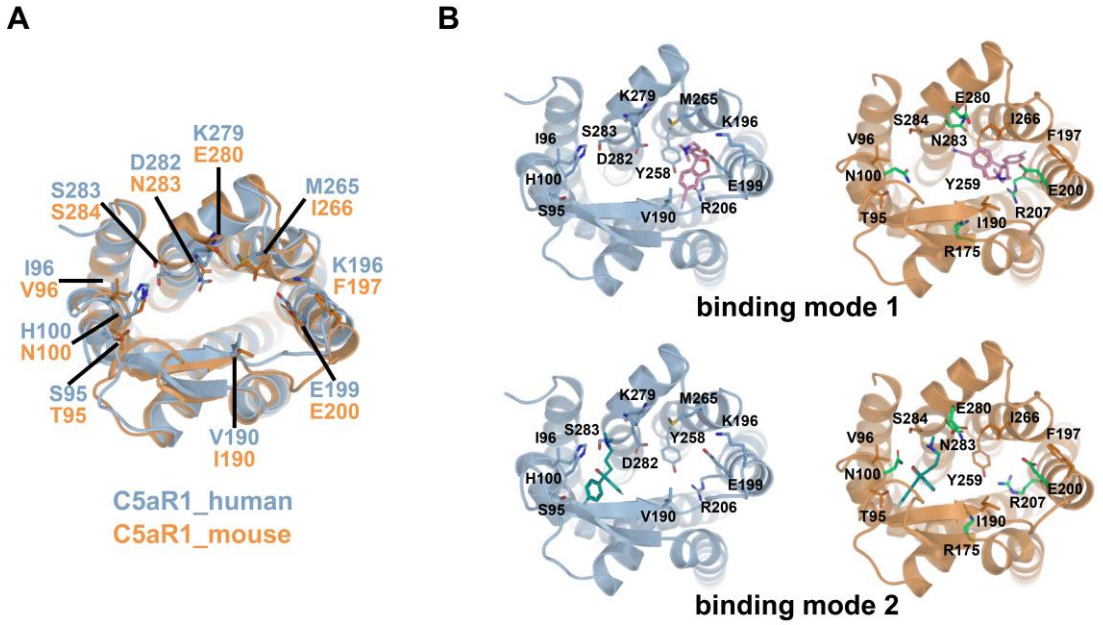

Figure S6. Predicted binding modes of citalopram to human and mouse C5aR1. (**A**) Conformations of orthosteric binding sites in human (light blue) and mouse (orange) C5aR1. The conformation of human C5aR1 was obtained from the crystal structure (PDB id: 6c1q). The structure of mouse C5aR1 was predicted using the ColabFold (AlphaFold2) software. (**B**) The predicted binding modes of citalopram to human (light blue) and mouse (orange) C5aR1. The conformations of citalopram were shown in pink (binding mode 1) or deep green (binding mode 2) sticks. For mouse C5aR1, green sticks indicate residues set to flexible in the molecular docking process.

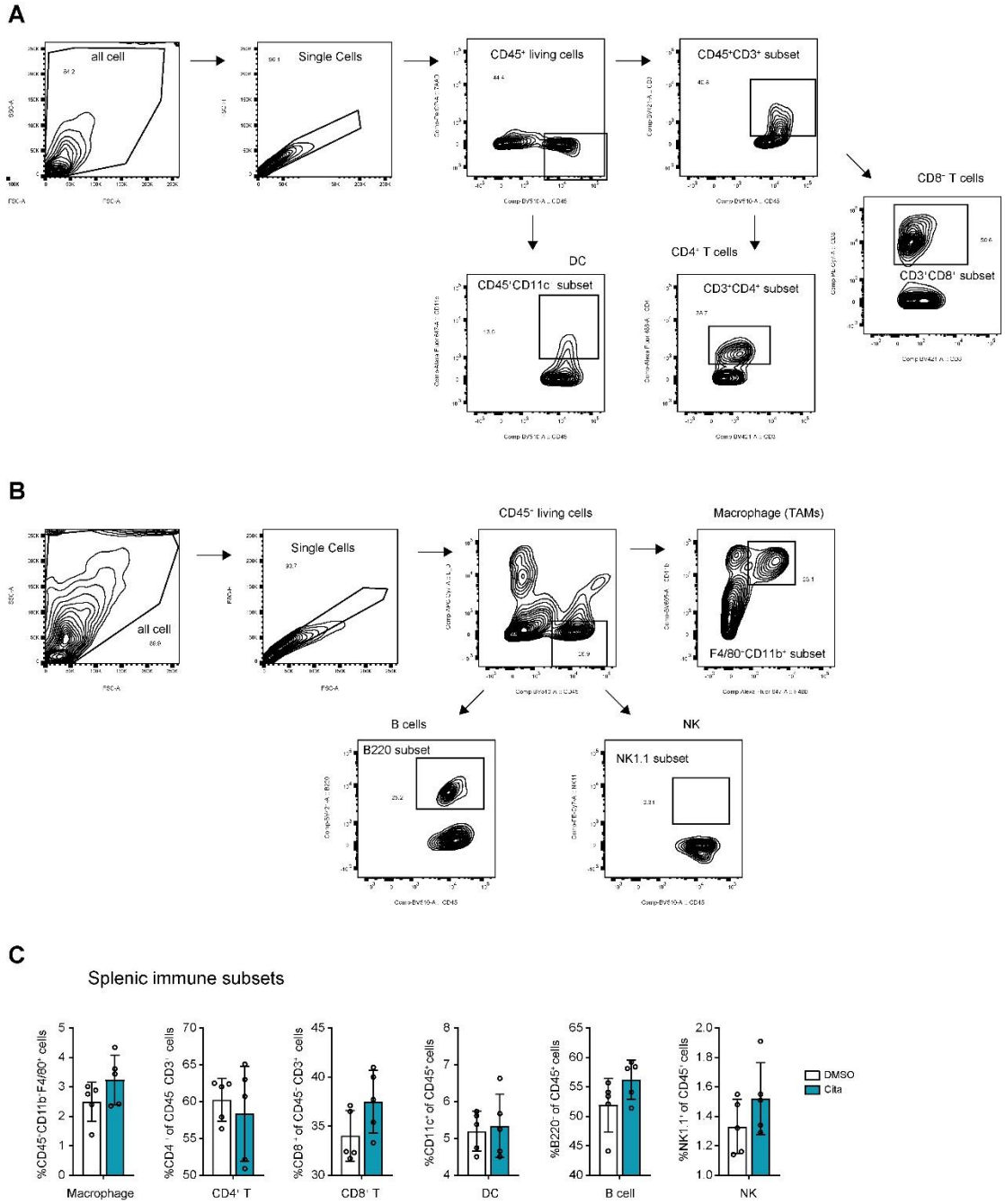

Figure S7. Flow cytometry analysis of immune cells in tumor tissues and spleen.

(**A**, **B**) Gating strategies used for flow cytometry analysis of tumor and splenic lymphocytes. Panel A: Identification of $CD4^+$ T cells, $CD8^+$ T cells, and dendritic cells (DC). Panel B: Identification of $B220^+$ B cells, tumor-associated macrophages (TAMs), and nature killer (NK) cells. (**C**) Flow cytometry showed the infiltration of $CD45^+CD11b^+F4/80^+$ macrophages, $CD4^+$ T cells, $CD8^+$ T cells, $B220^+$ B cells, $CD11c^+$ DC cells, and $NK1.1^+$ NK cells in spleen tissues from orthotopic xenograft model, which generated in immunocompetent C57BL/6 mice with Hepa1-6 cells (n = 5 per group). Values as mean ± SD and compared by the Student's t test.

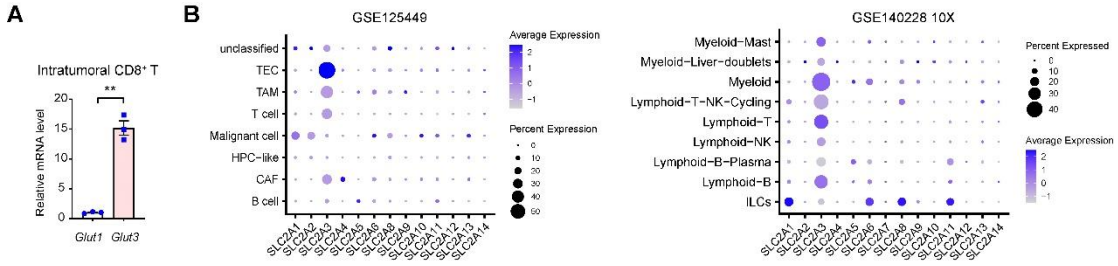

Figure S8. The expression pattern of Glut1 and Glut3 in CD8$^+$ T cells. (**A**) Real-time qPCR analysis of *Glut1* and *Glut3* expression in intratumoral CD8$^+$ T cells (n = 3 per group). (**B**) Single cell analysis of the expression of glucose transporter members in two HCC cohorts. Values as mean ± SD and compared by the Student's t test (**A**), $^{**}p < 0.01$.

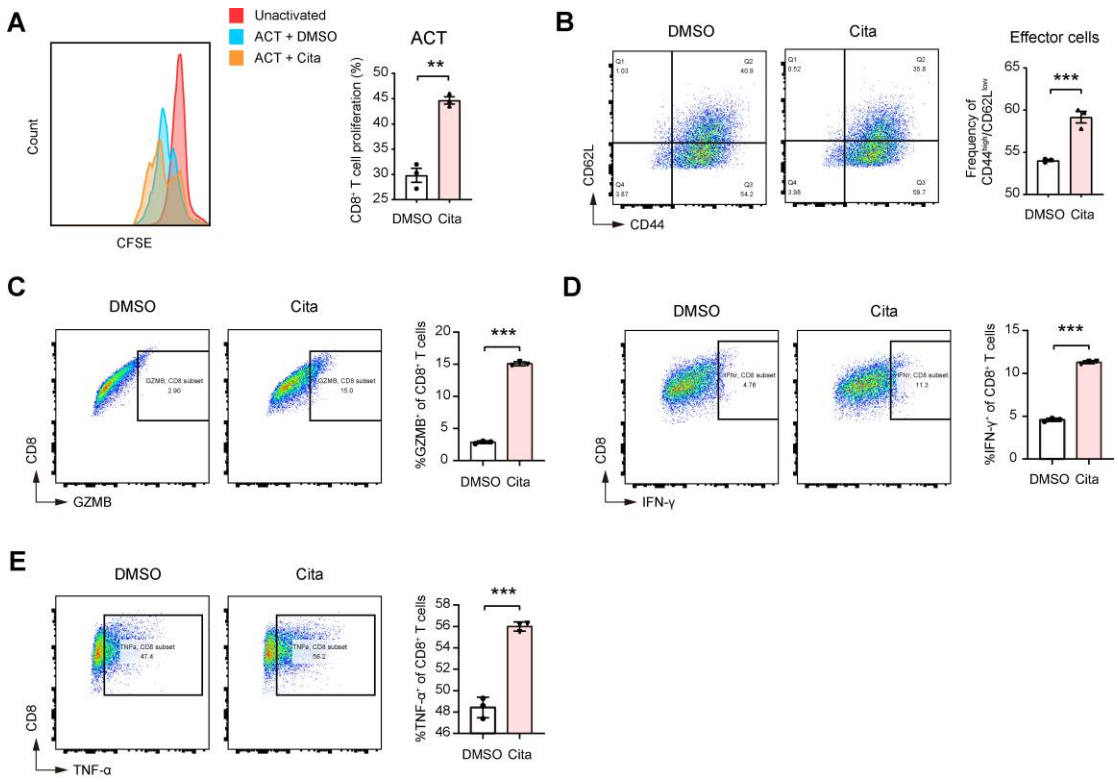

Figure S9. The *in vitro* effects of citalopram treatment on CD8$^+$ T cell function. (**A**) Splenic CD8$^+$ T cells isolated from C57BL/6 mice were stimulated with plate-bound α-CD3 plus α-CD28 for 72 h, and T-cell proliferation (CFSE staining) upon citalopram treatment was determined by flow cytometry (n = 3 per group); ACT: activated T cells. (**B**) Splenic CD8$^+$ T cells from C57BL/6 mice were stimulated with plate-bound α-CD3 and α-CD28 for 72 h, and CD44 and CD62L levels in activated CD8$^+$ T cells upon citalopram treatment were determined by flow cytometry (n = 3 per group). (**C**-**E**) Intracellular GZMB, IFN-γ, and TNF-α were detected in activated CD8$^+$ T cells upon citalopram treatment (n = 3 per group). In all panels, $^{**}p < 0.01$, $^{***}p < 0.001$. Values as mean ± SD and compared by the Student's t test.